

Application of MJO Simulation Diagnostics to Climate Models

D. Kim¹, K. Sperber², W. Stern³, D. Waliser⁴, I.-S. Kang¹, E. Maloney⁵,
S. Schubert⁶, W. Wang⁷, K. Weickmann⁸, J. Benedict⁵, M. Khairoutdinov⁹, M.-I. Lee^{6,10},
R. Neale¹¹, M. Suarez⁶, K. Thayer-Calder⁵, and G. Zhang¹²

¹Seoul National University, Atmospheric Science Program, Gwanak-gu, Seoul, 151-742, Korea

²Lawrence Livermore National Laboratory, PCMDI, P.O. Box 808, L-103, Livermore, CA 94550 USA

³NOAA Geophysical Fluid Dynamics Laboratory, P.O. Box 308, Princeton, NJ 08542 USA

⁴Jet Propulsion Laboratory, MS183-505 California Institute of Technology, 4800 Oak Grove Drive, Pasadena, CA 91109 USA

⁵Colorado State University, Department of Atmospheric Science, 1371 Campus Delivery, Fort Collins, CO 80523-1371 USA

⁶NASA Goddard Space Flight Center, 8800 Greenbelt Road, Greenbelt, MD 20771 USA

⁷NOAA National Centers for Environmental Prediction 5200 Auth Road, Camp Springs, MD 20746 USA

⁸NOAA/Earth System Research Laboratory, Physical Sciences Division, R/PSD1, 325 Broadway, DSRC-1D125 Boulder, CO 80305-3337 USA

⁹Stony Brook University, Institute for Terrestrial and Planetary Atmospheres, MSRC, Nicolls Road, Stony Brook, NY 11794-5000 USA

¹⁰Goddard Earth Sciences and Technology Center, University of Maryland Baltimore County, Baltimore, Maryland, 21250, USA

¹¹National Center for Atmospheric Research, P.O. Box 3000, Boulder, CO 80307-3000

USA

¹²Scripps Institution of Oceanography, 9500 Gilman Drive, Mail Code: 0221, La Jolla
CA, 92093 USA

J. Climate

January 2009

(submitted)

Corresponding author address: Daehyun Kim, School of Earth and Environmental
Sciences, Seoul National University, Seoul 151-747, South Korea

E-mail: kim@climate.snu.ac.kr

Abstract

The ability of eight climate models to simulate the Madden-Julian Oscillation (MJO) is examined using diagnostics developed by the US CLIVAR MJO Working Group. Though the MJO signal has been extracted throughout the annual cycle, this study focuses on the boreal winter (November-April) behavior. Initially, maps of the mean state and variance, and equatorial space-time spectra of 850hPa zonal wind and precipitation are compared with observations. Models best represent the intraseasonal space-time spectral peak in the zonal wind compared to that of precipitation. Using the phase-space of the multivariate principal components, the life-cycle properties of the simulated MJO's are extracted, including the ability to represent how the MJO evolves from a given subphase, and the associated decay time scales. On average, the MJO decay (e-folding) time scale for all models is shorter (~20-29days) than observations (~31days). All models are able to produce a leading pair of multivariate principal components that represents eastward propagation of intraseasonal wind and precipitation anomalies, although the fraction of the variance is smaller than observed for all models. In some cases, the dominant timescale of these PCs is outside of the 30-80 day band.

Several key variables associated with the model's MJO are investigated, including the surface latent heat flux, boundary layer (925hPa) moisture convergence, and the vertical structure of moisture. Frictional moisture convergence ahead (east) of convection supports eastward propagation in most of the models. A few models are also able to simulate the gradual moistening of the lower troposphere that precedes observed MJO convection, as well as the observed geographical difference in the vertical structure of moisture associated with the MJO. The dependence of rainfall on lower tropospheric relative humidity and the fraction of rainfall that is stratiform are also discussed, including implications these diagnostics have for MJO

simulation. Among models, the SPCAM and the ECHAM4/OPYC show the best skill at representing the MJO.

1. Introduction

More than three decades have passed since R. Madden and P. Julian published their pioneering discovery of tropical intraseasonal variability (Madden and Julian 1971; Madden and Julian 1972). Since then, many studies have been devoted to understanding the Madden-Julian Oscillation (MJO; e.g., Madden and Julian 1994; Zhang 2005) and predicting it using statistical and dynamical methods (Jones et al. 2000; Lo and Hendon 2000; Wheeler and Weickmann 2001; Jones et al. 2004; Seo et al. 2005; Waliser 2006; Vitart et al. 2007; Jiang et al. 2008). The MJO has been shown to impact a wide variety of climate phenomena across different spatial and temporal scales. Some examples include the onset and break of the Indian and Australian summer monsoons (e.g. Yasunari 1979; Wheeler and McBride 2005), the formation of tropical cyclones (e.g. Liebmann et al. 1994; Maloney and Hartmann 2000a; Maloney and Hartmann 2000b; Bessafi and Wheeler 2006) and onset of some El Niño events (e.g. Takayabu et al. 1999; Bergman et al. 2001; Kessler 2001). Hence, it is not possible to fully comprehend the above climate system components without knowledge of the MJO and its interactions with them (Lau and Waliser, 2005). Moreover, in a practical sense, accurate simulations and skillful predictions of the above phenomena may be difficult without the realistic representation of the MJO.

Numerous multi-model MJO intercomparison studies have been published over the past decade or so (Slingo et al. 1996; Waliser et al. 2003; Lin et al. 2006; Zhang 2006; Sperber and Annamalai 2008). The most significant message from the above studies is that GCMs continue to struggle to represent the MJO. Slingo et al. (1996) examined tropical intraseasonal variability using atmospheric GCM simulations forced by observed monthly mean sea-surface temperature (SST). They showed that the Atmospheric Model Intercomparison Project (AMIP) models were not able to simulate the observed 30-70 day spectral peak of the planetary scale (zonal

wavenumber 1) equatorial 200hPa velocity potential. Lin et al. (2006) analyzed MJO variability in 14 Coupled Model Intercomparison Project-3 (CMIP3) models that were a part of the Intergovernmental Panel for Climate Change (IPCC) assessment report 4 (AR4), and showed that only 2 models had MJO variance comparable to observations but with many other MJO features lacking realism. Regarding boreal summer intraseasonal variability, Waliser et al. (2003) analyzed AGCM simulations gathered by the International Climate Variability and Predictability (CLIVAR) monsoon panel. In their results, models did not realistically simulate eastward and northward propagation of precipitation seen in the observations. Recently, Sperber and Annamalai (2008) noted improvement in representing these aspects of the boreal summer intraseasonal variability in the CMIP3 models, especially the equatorial eastward propagation. However, much work remains to improve the MJO in climate models.

The afore-mentioned multi-model studies attempted to provide insight into what is important for MJO simulation by comparing the different physical parameterizations employed by models of differing MJO skill, though conflicting results arose. For example, Slingo et al. (1996) found that convection schemes closed on buoyancy tended to have stronger MJO variability, while Lin et al. (2006) suggested that models with moisture convergence closure had better MJO variability. This contradictory finding suggests that the ability of a GCM to simulate the MJO does not depend uniquely on its convective parameterization. Rather, it depends upon the complex interactions of convection with other physical processes in the model.

Even so, past studies have provided insight into the types of atmosphere model changes that lead to improved MJO simulations. These include (1) employing inhibition mechanisms associated with cumulus convection (Tokioka et al. 1988;

Wang and Schlesinger 1999; Lee et al. 2001; Maloney and Hartmann 2001; Maloney 2002; Lee et al. 2003; Zhang and Mu 2005a; Lin et al. 2008), (2) coupling to ocean models (Waliser et al. 1999; Hendon 2000; Kemball-Cook et al. 2002; Inness and Slingo 2003; Fu and Wang 2004; Sperber et al. 2005; Marshall et al. 2008), (3) improving the quality of the mean state MJO (e.g. Inness and Slingo 2003, Sperber et al. 2005), and (4) increasing vertical resolution (Inness et al. 2001; Jia et al. 2008). With regard to (1), by suppressing premature activation of deep convection, a model's subseasonal variability and MJO tend to be improved. Additionally, more realistic MJO may arise through an improved representation of downdrafts and rain re-evaporation (Maloney and Hartmann 2001) and modified convective closures (Zhang and Mu 2005a). Regarding items 2 and 3, the majority of studies find air-sea coupling to be beneficial for the simulation of the MJO, typically improving the periodicity and organization of MJO convection. However, MJO improvement due to air-sea interaction is predicated upon representing the proper phasing of surface flux exchanges and retaining a realistic mean state. In particular, simulating a realistic near-surface basic state westerly flow in the Indian and west Pacific Oceans appears important generating a realistic. Vertical resolution, item 4, has been shown to be important for MJO simulation as it improves the representation of the tri-modal distribution of clouds that is seen in observations (Johnson et al. 1999).

Since no uniform set of diagnostics has been used for assessing the quality of MJO simulations, it is tough to objectively determine the degree of improvement the modeling community has attained in simulating the MJO. With this in mind, US CLIVAR established the Madden-Julian Oscillation Working Group (MJOWG). A major goal of the MJOWG has been the development of a standardized set of diagnostics to evaluate MJO simulation in climate models (CLIVAR MJOWG 2008, <http://www.usclivar.org/mjo.php>). The MJOWG is encouraging the modeling

community to apply this hierarchy of diagnostics to their simulations to allow for a systematic comparison with other models. This paper is the first attempt to apply these diagnostics to climate model simulations. It is hoped that the current study will be the baseline for future intercomparison studies, and that this evaluation will be helpful in providing a more robust understanding of the MJO to aid future model development.

The models to which the diagnostics are applied are introduced in Section 2. In Section 3, the mean state, variance maps, and wavenumber-frequency spectra are examined. In Section 4, the combined EOF method of Wheeler and Hendon (2004) is used to investigate each model's own MJO and its life-cycle. The possible reasons for the diversity of simulations and deficiencies in each model's MJO simulation are discussed in Section 5, and Section 6 contains the summary and conclusions.

2. Model Simulations and Validation Data

a) Participating Models

The three coupled and five uncoupled GCM simulations used in this study were provided by MJOWG members and other interested parties. Basic aspects of the model configurations are given in Table 1, with more detailed descriptions available on the website: http://climate.snu.ac.kr/mjo_diagnostics/index.htm The models have various horizontal (from 2.8 to 1 degree) and vertical (from 19 to 72 levels) resolutions in their atmospheric components. Seven of the models are conventional GCMs in which convection and clouds are parameterized, while one model, superparameterized CAM (SPCAM), utilizes embedded 2-dimensional cloud resolving models for these processes (Khairoutdinov et al. 2005). The conventional GCMs all use mass flux type convection schemes in which the clouds are represented by single or multiple updrafts and downdrafts with the assumption of

steady-state clouds. These schemes have closures based on the release of convective available potential energy (CAPE, or cloud work function) when the parcel near cloud base is lifted to cloud top level. Typically, this method is based on “quasi-equilibrium” theory (Arakawa and Schubert 1974). In the theory, convection (sub-grid scale) quickly responds to large-scale (grid scale) forcing, with the release of CAPE (or cloud work function) triggered at a specified critical value. Two types of convective trigger functions are implemented in the models analyzed herein. The Tokioka modification (Tokioka et al. 1988), which suppresses convective plumes with entrainment rates less than a threshold that varies inversely with planetary boundary layer (PBL) depth, is implemented in CM2.1, GEOS5, and SNU. The constant α in Eq. (3) of Tokioka et al. (1988), which determines the strength of triggering, is largest in SNU (0.1) compared to that of CM2.1 (0.025) and GEOS5 (0.05). CAM3z and GEOS5 use a critical relative humidity (RH) value (Wang and Schlesinger 1999) at the parcel lifting level (CAM3z, 80%) and lifting condensation level (GEOS5, 30%), respectively. CAM3z uses a modified closure compared to standard CAM (Zhang and Mu 2005b), called free tropospheric quasi-equilibrium in which convection removes CAPE generated by free tropospheric processes. CAM3.5 uses a modified calculation of CAPE whereby the reference parcel calculation is allowed to entrain (Neale et al. 2008).

b) Observation Data

We validate the simulations against the Advanced Very High Resolution Radiometer outgoing longwave radiation (OLR, Liebmann and Smith 1996) which is a proxy of convective activity. We use rainfall from the Climate Prediction Center Merged Analysis of Precipitation (CMAP, Xie and Arkin 1997) and the Global Precipitation Climatology Project (GPCP, Huffman et al. 2001). For monthly total and

stratiform rainfall amounts we use the 3A25 product from the Tropical Rainfall Measuring Mission (TRMM, Kummerow et al. 2000). The upper (200hPa) and lower (850hPa) tropospheric zonal winds are from NCEP/NCAR reanalysis data (Kalnay et al. 1996). The structures of specific humidity, surface latent heat flux, and 925hPa moisture convergence based on European Centre for Medium-range Weather Forecasts (ECMWF) 40-Year reanalysis (ERA40, Uppala et al. 2005) are included in our analysis, since Tian et al. (2006) has indicated possible shortcomings in the MJO-relevant specific humidity fields from the NCEP/NCAR reanalysis. For the surface latent heat flux we also use the objectively analyzed air-sea fluxes (OAFlux) from Yu and Weller (2007).

A wider variety of data sources have been employed to assess observational uncertainty, though their presentation is beyond the scope of this paper. These additional diagnostics, which support the conclusions of this paper, are available via the MJO Working Group website: <http://www.usclivar.org/mjo.php> or more directly from the model analysis website http://climate.snu.ac.kr/mjo_diagnostics/index.htm

3. Diagnostic Strategy and Basic Diagnostics

a) Diagnostic Strategy

The MJOWG has assembled two levels of MJO diagnostics of increasing complexity, plus the evaluation of mean state variables that have been implicated as being directly related to MJO simulation skill (CLIVAR MJOWG 2008). Although the MJOWG developed diagnostics for both boreal summer and winter, for the sake of brevity, we will concentrate only on the boreal winter season (November to April). However, diagnostics of boreal summer intraseasonal variability (May to October) are also presented and discussed in CLIVAR MJOWG (2008) and

illustrated on the simulation diagnostics website. As a crucial starting point, the mean state of relevant variables, some of which have been discussed in section 1, are first validated. Level 1 diagnostics assess the dominant spatial and temporal scales, as well as propagation direction of precipitation and 850hPa zonal wind. Because these diagnostics only provide a general evaluation in terms of mean state and broad-band intraseasonal variability, level 2 diagnostics are employed to extract and evaluate the MJO using multivariate EOF analysis. Defining MJO phases from the leading PCs, the temporal persistence of model MJO amplitude as a function of subphase is compared with observations. Finally, MJO life cycle composites of moist variables are derived to gauge the realism of each model's simulated fields, but also gain insight into the mechanism by which the MJO is maintained.

b) Mean State

Figure 1 shows the mean state of the 850hPa zonal wind and precipitation. Though some pronounced mean state biases exist, both models and observations suggest that high mean precipitation ($>11 \text{ mm day}^{-1}$) in the west Pacific is associated with the eastward extension of the westerly zonal wind into that basin. Over the tropical western Pacific Ocean the mean state of the 850hPa zonal wind has been shown to be indicative of the ability of a model to represent MJO convection over this region (e.g. Inness et al. 2003; Sperber et al. 2005). Of the models analyzed herein, only CFS does not bear out this relationship, though in this model the strongest MJO convective signal is incorrectly located over the Eastern Hemisphere.

The results from the mean state diagnostics are summarized in Fig. 2. The scatter diagrams of pattern correlation vs. normalized root mean square error (NRMSE) over the west Pacific and Indian Oceans are used as metrics to assess mean state skill. Higher pattern correlations and lower NRMSE are desirable. There is no

model which is the best for all the variables. For example, while ECHAM4/OPYC, which uses annual mean flux adjustment of heat and moisture, shows superior skill in simulating low level wind (Fig. 2b), it is in the middle of the populations for OLR (Fig. 2b) and upper level wind (Fig. 2d).

c) 20-100 Day Filtered Variance

To see how the magnitude and geographical distribution of sub-seasonal variability are simulated, we show maps of the 20-100 day filtered variance of U850 and precipitation (Fig. 3). In observations (Fig. 3a), the U850 and precipitation variance maxima are located in eastern Indian Ocean, western Pacific and south of Maritime Continent region. The intraseasonal variability of both U850 and precipitation is weak over the Maritime Continent. These attributes are most realistically represented in CAM3z, ECHAM4/OPYC, SNU, and SPCAM (Figs. 3c, 3f, 3h, and 3i). CAM3z and SPCAM configurations demonstrate an improved intraseasonal variance pattern compared to the current standard version of the model, CAM3.5 (Fig. 3b), although they have variance much higher than observed. Earlier versions of the CAM model also exhibited difficulty in simulating intraseasonal variations (Sperber 2004) and other modifications of the convection scheme in CAM have led to improved intraseasonal behavior (Maloney and Hartmann 2001; Liu et al. 2005; Zhang and Mu 2005a). Both the GEOS-5 and CAM3.5 have weaker than observed precipitation variance.

As noted in Figs. 2e and 2f, comparison of Figs. 1 and 3 indicates the observed pattern correlation between the mean state and intraseasonal variance is generally higher for precipitation (0.78) than U850 (0.37). In comparison, averaged values over the simulations are 0.79 (precipitation) and 0.29 (U850), suggesting that models can reproduce this behavior. Additionally, there is a correspondence between the

strength of simulated South Pacific Convergence Zone (SPCZ) and the strength of sub-seasonal variability. For CAM3z, CM2.1, ECHAM4/OPYC, SNU, and SPCAM, the SPCZ rainfall is larger than observed, and these models all have stronger than observed sub-seasonal variance. This result is consistent with the model results of Slingo et al. (1996), with the SPCZ signal possibly being related to Rossby wave propagation induced by MJO convection (Matthews et al. 1996).

d) Wavenumber-Frequency Spectra

In Fig. 4 we use equatorial wavenumber-frequency plots (Hayashi 1979) of precipitation and U850 to isolate the characteristic spatial and temporal scales on which variability is organized. Consistent with the results of previous studies (Weickmann et al. 1985; Kiladis and Weickmann 1992; Zhang et al. 2006), the dominant spatial scale of precipitation in observations is zonal wavenumbers 1 to 3 and for U850 it is zonal wavenumber 1 for periods of 30-80 days (Fig. 4a). These scales distinguish the MJO from other convectively coupled equatorial waves (Wheeler and Kiladis 1999).

For U850, ECHAM4/OPYC produces a spectrum similar to observation (Fig. 4f), whereas CFS and SPCAM overestimate the power for periods of 30 to 80 days (Figs. 4d and 4i). For CAM3.5 and CM2.1, the eastward propagating power tends to be concentrated at low-frequencies (period > 80 days; Figs. 4b and 4e). Compared to U850, most models are less successful at representing the 30-80 spectral peak for precipitation models (CAM3.5, CFS, CM2.1, ECHAM4/OPYC, GEOS5, and SNU). Consistent with Zhang et al. (2006), these results suggest a lack of coherence between the simulation of intraseasonal precipitation and U850.

An important metric derived from the wavenumber-frequency spectra is the east-west ratio of MJO spectral power shown in Fig. 5. In observations the east-west

power ratio is $\sim 3-4$ for precipitation and U850. For U850 three (five) of the models have larger (smaller) ratios compared to observation. Our precipitation power ratios are consistent with Lin et al. (2006), who showed that most of the Coupled Model Intercomparison Project-3 (CMIP3) models have a smaller east/west ratio than observed (their Fig. 10).

4. MJO Modal Analysis

In previous studies, the MJO has been isolated using empirical orthogonal function (EOF) analysis using different variables, such as velocity potential (e.g. Lau and Lau 1986; Knutson and Weickmann 1987), relative vorticity (e.g. Annamalai et al. 1999), winds (e.g. Gutzler and Madden 1989; Maloney and Hartmann 1998; Sperber et al. 2000), and OLR (e.g. Hendon and Glick 1997; Sperber 2003; Sperber et al. 2005). As such, direct comparison of MJO quality in models based on the use of different variables for isolating the MJO is not possible.

We use the CLIVAR MJOWG (2008) Level 2 multivariate combined EOF (CEOF) technique developed by Wheeler and Hendon (2004, hereafter WH04) in which OLR, U850, and U200 are used to extract the MJO modes. This multivariate approach isolates the convective and baroclinic zonal wind signature of the MJO. The study of WH04 used unfiltered input data to the CEOF analysis to develop a real-time MJO diagnostic for their experimental MJO forecast system, whereas we use 20-100 day bandpass filtered data to facilitate isolating the MJO modes. We specifically focus on the evaluation of 1) significant separation of the leading CEOFs from the higher modes, 2) the similarity of the model eigen vector pairs with observed patterns, 3) determination of the dominant time scale of the MJO PCs, and 4) the mean coherence squared between the leading PC's at the MJO time scale (30~80 days).

a) MJO Mode from CEOF Analysis

The first two CEOF eigen vectors are shown in Fig. 6. In observations (Fig. 6a), the leading CEOF's explain more than 43% of the filtered variance. These MJO modes capture the enhanced convective activity over the Maritime continent (Fig. 6a, upper) and the Indian ocean/west Pacific (Fig. 6a, lower), and together they constitute the eastward propagating MJO. As seen in these figures, the upper and lower troposphere zonal winds are out of phase with one another, thus demonstrating the baroclinic structure of the MJO. Additionally, there is a signal displacement of the zonal wind maxima relative to the convection signal with low-level easterlies (westerlies) tending to lead (trail) the convective maximum.

The match between the simulated and observed modes is objectively determined by examining pattern correlations between observed and simulated eigen vectors (Fig. 6). The pattern correlations range from 0.64 (CAM3z, upper mode) to ≥ 0.8 for CAM3.5, CFS, CM2.1, ECHAM4/OPYC, and SPCAM, suggesting good agreement with observations in representing the MJO spatial patterns, especially for the latter models. Except for CM2.1, the two leading modes are statistically distinguishable from the higher order modes, as in observations, though the percent variance explained by the models is smaller than observed. The phase difference (not shown) between the PC's is nearly 90 degrees, which means the upper panel leads lower panel by 1/4 cycle for observations and all models. For the models, the baroclinic zonal wind signature is better represented than the convective pattern. For example, the CFS has maximum convective amplitude with CEOF1 in the Western Hemisphere, whereas in observations the maximum amplitude is in the Eastern Hemisphere.

To assess if the extracted MJO modes are physically meaningful and distinct from a rednoise process we calculate power spectra of unfiltered PC's. The unfiltered

PC's are obtained by projecting the leading CEOF's in Fig. 6 onto unfiltered data (with only the seasonal cycle removed). If the power spectra of the unfiltered PC's, shown in Fig. 7, yield a statistically significant peak at MJO time scales, then we have increased confidence that the extracted MJO modes are real. In observations (Fig 7a), statistically significant spectral power at the 99% confidence level relative to a rednoise process is concentrated at periods of 30 to 80 days. CFS, ECHAM4/OPYC, and SPCAM (Figs. 7d, 7f, and 7i) best represent the observed time scale, although the power is model dependent. This analysis clearly highlights the benefit to using a multiple diagnostic technique to analyze an MJO simulation. While the CFS here appears to produce an observed PC spectrum superior to some other models, the diagnosed spatial structure of the leading CEOFs indicates that its MJO has significant biases relative to observations. Of the remaining models, CAM3.5, CAM3z, and SNU (Figs. 7b, 7c, and 7h) having the largest variance at periods less than 30 days, while CM2.1 (Fig. 7e) is dominated by excessive power at low frequencies.

b) MJO Life Cycle Evolution

Plotting PC-1 vs. PC-2 we evaluate the phase-space evolution of the MJO life-cycle. For each of 8 subphases we composite 40 day segments that start from that subphase which have an initial MJO amplitude $(PC1^2+PC2^2)^{1/2}$ larger than 1.5. In observations, Fig. 8a, the amplitude decays as the MJO life-cycle evolves, finally crossing the unit variance circle into the realm that we refer to as a "Weak MJO." As shown in Table 2, the average e-folding decay time over all initial subphases is ~31 days for observations, with all models having a faster decay time scale (~20-29 days). The shape of the phase-space spiral is dependent upon two factors; (1) the ability of the model to evolve an MJO, and (2) the preferred period of the MJO. For example,

CAM3.5 and CM2.1 have nearly identical decay times, but the CM2.1 phase-space plot (Fig. 8e) displays a more open spiral compared to that of CAM3.5 (Fig. 8b). This arises because the preferred MJO time scale in CM2.1 is about 80 days (Fig. 7e), while that of CAM3.5 is about 25 days (Fig. 7b). Thus, CM2.1 evolves through fewer MJO life-cycle subphases compared to CAM3.5, as the MJO amplitude of both decays on nearly the same time scale.

c) MJO Life Cycle Composite

MJO life cycle composites are constructed by averaging band pass filtered anomalies across all days that fall within a given phase when the MJO amplitude is greater or equal to 1. We evaluate OLR, surface latent heat flux, 925hPa moisture convergence, and the vertical specific humidity profile at three different longitudes.

Figure 9 shows phase-longitude diagrams of OLR and surface latent heat flux anomalies. Observations show two convective maxima (Fig. 9a), one over the eastern Indian Ocean and the other over the west Pacific Ocean with weakened convection over the Maritime Continent. The strong convective signal is preceded by a negative evaporation anomaly while positive evaporation anomalies follow the enhanced convection. Models generally capture this relationship although the amplitude of the evaporation anomaly associated with convection is especially weak in CAM3.5 and GEOS5 (Figs. 9b and 9g) in which the convective anomalies exhibit little or no eastward propagation. Contrary to observations, the CFS model (Fig. 9d) has its largest latent heat flux signal over the eastern Pacific Ocean, and largest OLR amplitude in the Atlantic.

Frictional wave-CISK has been hypothesized as a mechanism of maintaining the MJO in many theoretical (Wang 1988; Salby et al. 1994), observational (Salby et al. 1994; Salby and Hendon 1994; Maloney and Hartmann 1998; Sperber 2003) and

modeling (Lee et al. 2003; Sperber et al. 2005) studies. This theory requires frictional moisture convergence within the planetary boundary layer east of the deep convection. In Fig. 10, we plot a longitude-phase diagram of OLR and 925hPa moisture convergence anomalies for observations and models. Due to quality concerns of the NCEP reanalysis moisture field (Tian et al. 2006), the result from ERA40 is also plotted (Fig. 10f). Over the eastern hemisphere the MJO 925hPa moisture convergence anomalies from NCEP are weaker than those from ERA40, with NCEP anomalies extending further east into the central and eastern Pacific (Figs. 10a and 10f). All simulations show low-level moisture convergence leading the enhanced MJO convection. CAM3.5, CAM3z, SNU, and SPCAM (Figs. 10b, 10c, 10i, and 10j) exhibit the extension of the moisture convergence anomalies into the central and eastern Pacific, akin to NCEP/NCAR reanalysis. Conversely, CFS, CM2.1, and ECHAM4/OPYC (Figs. 10d, 10e, and 10g), are most similar to ERA40, with the moisture convergence signal mostly confined to the warm pool region (40°E-160°E).

The equatorial vertical structure of the MJO has been examined in a number of studies (Rui and Wang 1990; Myers and Waliser; 2003; Sperber 2003; Kiladis et al. 2005; and Tian et al. 2006). Figure 11 presents MJO life cycle composites of the vertical structure of ERA-40 specific humidity at three different longitudes, the Indian Ocean (80°E, left), west (130°E, middle) and east Pacific Ocean (140°W, right). In observations, Figs. 11a and 11f, the low-level moistening precedes enhanced convection over the warm pool longitudes (80°E and 130°E). The slope of the vertical tilt depends on the longitude, consistent with the findings of Sperber (2003) and Kiladis et al. (2005). In the warm pool longitudes, the peak level for the specific humidity anomaly occurs at about 600hPa when the convection is strongest. As in observations, the vertical structure of moisture associated with the MJO depends on the geographical location in all models. However, the models do exhibit some

significant differences from observations. For example, in CAM3.5 the mid- to upper-tropospheric moisture anomalies are apparent, but only a weak signal exists in lower troposphere, especially in the warm pool region (Figs. 11a and 11b). CFS, ECHAM4/OPYC, and SPCAM give the most realistic simulations of moisture anomalies associated with the MJO (Figs. 11d, 11g, and 11j).

5. Discussion

The MJOWG diagnostics presented in Sections 3 and 4 assess the ability of the models to represent the MJO. While these diagnostics point to shortcomings in the ability of models to simulate the MJO, they do not directly indicate which physical processes are most important and/or responsible for the quality of the MJO. This issue was a topic of considerable discussion at a recent CLIVAR-sponsored MJO workshop (Sperber and Waliser, 2008), with the recommendation that in addition to the diagnostics established to date, more process-oriented diagnostics should be explored and developed in the future. In this section, we make an initial attempt towards this objective.

If we consider the coherence-squared of PC-1 vs. PC-2 in the intraseasonal band as a metric of MJO simulation skill (Fig. 6), we can relate it to basic aspects of model performance, in this case the quality of the time-mean state of key variables (Fig. 12). Only for precipitation is there a 5% significant direct relationship between MJO skill and the time-mean state. This suggests two possibilities; (1) one must have good mean state background of precipitation in order to have the potential to represent the MJO, or (2) representing a reasonable spectrum of precipitation variability (including the MJO) is the proper way to attain a realistic mean state (e.g., Waliser et al. 2003). Irrespective of which possibility is correct, further investigation of precipitation and moist processes is warranted, since these may have a bearing on the ability to

represent the MJO.

In order to gain some insight on precipitation and moist processes, in Fig. 13 we plot the vertical profile of relative humidity (RH) versus precipitation intensity. This diagnostic has previously proven useful for gaining insight into the superior ability of SPCAM to simulate the MJO relative to CAM3.0 (Thayer-Calder 2008, Thayer-Calder and Randall 2009). In the observations (GPCP precipitation and ERA-40 RH, Fig. 13a), RH in the troposphere gradually increases with increasing precipitation, and it becomes nearly constant throughout the troposphere when the rainfall amount is larger than about 70 mm/day. This implies that heavy rainfall is inhibited until the column is sufficiently moistened. In the models the column is too dry in models when precipitation is weak. In observations RH of 95% are rarely obtained (Fig. 13a), while the models produce excessive RH near the tropopause when the precipitation rate is larger. This error extends to the middle-lower troposphere in all models except ECHAM4/OPYC (Fig. 13e). Since this model also has one of the better representations of the MJO, our result lends support to tropospheric moisture control on precipitation events as an important process in the simulating the MJO.

To correctly represent the life-cycle of precipitation processes, another important consideration is the adequate representation of stratiform rainfall. Using recently released precipitation and latent heat estimates from TRMM, Morita et al. (2006) and Benedict and Randall (2007) showed that shallow and congestus cumulus prevail in the early stages of MJO related convective activity, while deep cumulonimbus and stratiform clouds dominate during the peak and decaying stages. Lin et al. (2004) showed the important role of stratiform rainfall in producing a top-heavy vertical heating structure associated with the observed MJO, and Dai (2006) showed that many GCMs suffer from the lack of stratiform rainfall compared to observation. In observations about 40% of total precipitation in tropics is in the form of stratiform

rainfall (Schumacher and Houze 2003). The annual mean stratiform rainfall fraction, presented in Fig. 14a based on the TRMM 3A25 product, has a lower stratiform rain fraction compared to the analysis of Schumacher and Houze (2003) who used the TRMM 2A23 product. Nevertheless, CAM3.5 and CAM3z (Figs. 14b and 14c) still have a smaller fraction of stratiform rainfall compared to TRMM 3A25 product. ECHAM4/OPYC (Fig. 14d) is most similar to observations in terms of pattern and fraction over near equatorial Indian Ocean and western Pacific, key areas of MJO convective propagation, but elsewhere the fraction is overestimated. SNU also produces similar stratiform rain fractions compared to observations. However, when its trigger function is turned off, SNU has a reduced stratiform rainfall ratio (Fig. 14f), and the troposphere is too dry (Fig. 13g). The subseasonal variability and the MJO are better simulated by the SNU model with the convective trigger implemented (Lin et al. 2008).

For ECHAM4/OPYC model, the results in Figs. 13 and 14 indicate that a model with a good MJO also exhibits a realistic representation of precipitation rate vs. relative humidity, and the partitioning of stratiform vs. convective rainfall. The other models, which have poorer MJO's, exhibit less consistency in their ability to represent these experimental diagnostics. Regarding the MJO, these may not be cause and effect relationships, but such a multivariate validation approach is at least useful to suggest where inconsistencies arise with respect to the model physics and observations.

6. Summary and Conclusions

Standardized MJO diagnostics, developed by the CLIVAR MJOWG (CLIVAR MJOWG 2008; http://climate.snu.ac.kr/mjo_diagnostics/index.htm), have been applied to eight climate model simulations. Mean state, variance maps, and

wavenumber-frequency diagrams are used to evaluate each model's sub-seasonal variability of U850 and precipitation, and their relationship to the model climatology. Generally the MJO signal in the large-scale circulation (U850) is better represented than in convection (precipitation). The subseasonal variability of precipitation and U850 is stronger than observed in the majority of GCMs (Fig. 3). Each model's MJO is extracted using 200 hPa and 850 hPa zonal wind and OLR in the combined EOF method of WH04. All models produce a leading pair of CEOFs that represent eastward propagating zonal wind variability resembling observations, although OLR structures associated with these CEOFs differ significantly from observations in some models. The leading CEOFs uniformly explain less of the variance in the models than observations. Often, the dominant timescale of the model MJO modes is outside of the 30-80 day band. The persistence of strong MJO events is shorter in models than observations. Consistent with the observations as analyzed by WH04, the multivariate CEOF method is better than univariate EOF analysis in capturing MJO-like phenomena in climate simulations based on using the coherence-squared of PC-1 vs. PC-2 in the intraseasonal band as a metric of MJO performance (not shown).

Based on community recommendations at a recent MJO workshop (Sperber and Waliser, 2008), a number of additional process-oriented diagnostics are considered. Negative surface latent heat flux anomalies to the east of the convective anomalies are seen in most of the models with strong MJO signals. Positive moisture convergence anomalies within the PBL (925hPa) preceding enhanced convection appear in most of the simulations, supporting the frictional wave-CISK mechanism (Wang 1988; Salby et al. 1994). However, most of the GCMs show errors in the vertical structure of moisture anomalies as a function of MJO phase. Many models do not show the low-level preconditioning of the troposphere that precedes

observed convective events. This inability of model moist physics to correctly represent the sensitivity of precipitation to the vertical structure of tropospheric relative humidity cites the need for improved convective parameterizations. Finally, another diagnostic measure of a GCM's treatment of convection, the ratio of stratiform rainfall to total precipitation is quite varied among the models used here, and their similarity to observations is typically poor.

SPCAM and ECHAM4/OPYC show relatively better skill in representing the MJO than the other models. The results indicate that a good MJO simulation is possible through the use of conventional parameterization and by explicitly resolving clouds at each grid point (cf. Miura et al. 2008; Sperber et al. 2008). ECHAM4/OPYC has a quite good mean state of precipitation and low level wind, noting that annual mean flux adjustment of heat and fresh water were applied to the simulation, which may contribute to the realistic intraseasonal variability in this model (Sperber et al. 2005). Interestingly, diabatic heating (rainfall) is a more difficult variable to simulate than the large scale circulation field (U850). Because these variables are closely linked, comparable skill would have been expected. To resolve this paradox, and to gain further insight into the process/interactions that are required to enable simulation of the MJO it will be necessary to archive vertical profiles of the diabatic heating components at a frequent enough sampling (or averaging) rate (e.g., at least 1/day) to gain new insight into the convective interactions necessary for MJO simulation. The approach calls for the use of a hierarchy of models (parameterized through cloud-resolving models) along with suitable observations, so that improved parameterizations of convective processes in climate models can be realized. A more realistic representation of the spectrum of variability in climate models will provide a better estimate of how climate extremes will change due to anthropogenic climate change.

Acknowledgements. K. Sperber was supported under the auspices of the U.S. Department of Energy Office of Science, Climate Change Prediction Program by Lawrence Livermore National Laboratory under contract DE-AC52-07NA27344. D. Waliser's contributions to this study were carried out on behalf of the Jet Propulsion Laboratory, California Institute of Technology, under a contract with the National Aeronautics and Space Administration (NASA). E. Maloney was supported by the Climate and Large-Scale Dynamics program of the NSF under grant ATM-0832868, and under Award# NA050AR4310006 from the National Oceanic and Atmospheric Administration. We thank Dr. M. Wheeler (Centre for Australian Weather and Climate Research) and Prof. B. Wang (University of Hawaii) for helpful comments.

REFERENCES

- Annamalai, H., J. M. Slingo, K. R. Sperber, and K. Hodges, 1999: The Mean Evolution and Variability of the Asian Summer Monsoon: Comparison of ECMWF and NCEP/NCAR Reanalyses. *Mon. Wea. Rev.*, **127**, 1157-1186.
- Arakawa, A. and W. H. Schubert, 1974: Interaction of a Cumulus Cloud Ensemble with the Large-Scale Environment, Part I. *J. Atmos. Sci.*, **31**, 674-701.
- Benedict, J. J., D. A. Randall, 2007: Observed characteristics of the MJO relative to maximum rainfall. *J. Atmos. Sci.*, **64**, 2332-2354
- Bergman, J. W., H. H. Hendon, and K. M. Weickmann, 2001: Intraseasonal Air-Sea Interactions at the Onset of El Nino. *J. Climate*, **14**, 1702-1719.
- Bessafi, M. and M. C. Wheeler, 2006: Modulation of South Indian Ocean Tropical Cyclones by the Madden-Julian Oscillation and Convectively Coupled Equatorial Waves. *Mon. Wea. Rev.*, **134**, 638-656.
- CLIVAR Madden-Julian Oscillation Working Group, 2008: MJO simulation diagnostics. *J. Climate*, (accepted)
- Dai, A., 2006, Precipitation Characteristics in Eighteen Coupled Climate Models, *J. Climate*, **19**, 4605-4630
- Delworth, T. L., and Coauthors, 2006: GFDL's CM2 global coupled climate models. Part 1: Formulation and simulation characteristics. *J. Climate*, **19**, 643-674.
- Fu, X., and B. Wang, 2004: Differences of boreal-summer intraseasonal oscillations simulated in an atmosphere-ocean coupled model and an atmosphere-only model., *J. Climate*, **17**, 1263-1271.
- Gutzler, D. S. and R. A. Madden, 1989: Seasonal Variations in the Spatial Structure of Intraseasonal Tropical Wind Fluctuations. *J. Atmos. Sci.*, **46**, 641-660.
- Hayashi, Y., 1979: A Generalized Method of Resolving Transient Disturbances into Standing and Traveling Waves by Space-Time Spectral Analysis. *J. Atmos. Sci.*, **36**,

1017-1029.

Hendon, H. H., 2000: Impact of air-sea coupling on the Madden-Julian oscillation in a general circulation model. *J. Atmos. Sci.*, **57**, 3939-3952.

Hendon, H. H. and J. Glick, 1997: Intraseasonal Air-Sea Interaction in the Tropical Indian and Pacific Oceans. *J. Climate*, **10**, 647-661.

Hendon, H. H., 2000: Impact of air-sea coupling on the Madden-Julian Oscillation in a general circulation model. *J. Atmos. Sci.*, **57**, 3939-3952.

Hong, S.-Y., and H.-L. Pan: Convective Trigger Function for a Mass-Flux Cumulus Parameterization Scheme. *Mon. Wea. Rev.*, **126**, 2599-2620..

Huffman, G. J., R. F. Adler, M. M. Morrissey, D. T. Bolvin, S. Curtis, R. Joyce, B. McGavock, and J. Susskind, 2001: Global precipitation at one-degree daily resolution from multisatellite observations. *J. Hydrometeor.*, **2**, 36-50.

Inness, P. M. and J. M. Slingo, 2003: Simulation of the Madden-Julian oscillation in a coupled general circulation model. Part I: Comparison with observations and an atmosphere-only GCM. *J. Climate*, **16**, 345-364.

Inness, P. M., J. M. Slingo, E. Guilyardi, and J. Cole, 2003: Simulation of the Madden-Julian oscillation in a coupled general circulation model. Part II: The role of the basic state. *J. Climate*, **16**, 365-382.

Inness, P. M., J. M. Slingo, S. J. Woolnough, R. B. Neale, and V. D. Pope, 2001: Organization of tropical convection in a GCM with varying vertical resolution; implications for the simulation of the Madden-Julian Oscillation. *Climate Dyn.*, **17**, 777-793.

Jia, X., C. Li, J. Ling, and C. Zhang, 2008: Impacts of a GCM's resolution on MJO simulation. *Advances in Atmospheric Sciences*, **25**, 139-156.

Jiang, X., D. E. Waliser, M. C. Wheeler, C. Jones, M.-I. Lee, and S. D. Schubert, 2008: Assessing the Skill of an All-season Statistical Forecast Model for the Madden-

- Julian Oscillation. *Mon. Wea. Rev., Mon. Wea. Rev.*, **136**, 1940-1956.
- Johnson, R. H., T. M. Rickenbach, S. A. Rutledge, P. E. Ciesielski, W. H. Schubert, 1999: Trimodal characteristics of tropical convection. *J. Climate*, **12**, 2397-2418
- Jones, C., D. E. Waliser, J. K. E. Schemm, and W. K. M. Lau, 2000: Prediction skill of the Madden and Julian Oscillation in dynamical extended range forecasts. *Climate Dyn.*, **16**, 273-289.
- Jones, C., L. M. V. Carvalho, R. Wayne Higgins, D. E. Waliser, and J. K. E. Schemm, 2004: A Statistical Forecast Model of Tropical Intraseasonal Convective Anomalies. *J. Climate*, **17**, 2078-2095.
- Kalnay, E., M. Kanamitsu, R. Kistler, W. Collins, D. Deaven, L. Gandin, M. Iredell, S. Saha, G. White, J. Woollen, Y. Zhu, M. Chelliah, W. Ebisuzaki, W. Higgins, J. Janowiak, K. C. Mo, C. Ropelewski, J. Wang, A. Leetmaa, R. Reynolds, R. Jenne, and D. Joseph, 1996: The NCEP/NCAR 40-year reanalysis project. *Bull. Amer. Meteor. Soc.*, **77**, 437-471.
- Kemball-Cook, S., B. Wang, and X. Fu, 2002: Simulation of the ISO in the ECHAM4 model: The impact of coupling with an ocean model. *J. Atmos. Sci.*, **59**, 1433-1453.
- Kessler, W. S., 2001: EOF representations of the Madden-Julian oscillation and its connection with ENSO. *J. Climate*, **14**, 3055-3061.
- Khairoutdinov, M., D. Randall, and C. DeMott, 2005: Simulations of the Atmospheric General Circulation Using a Cloud-Resolving Model as a Superparameterization of Physical Processes. *J. Atmos. Sci.*, **62**, 2136-2154.
- Khairoutdinov, M., D. Randall, 2003, Cloud Resolving Modeling of the ARM Summer 1997 IOP: Model Formulation, Results, Uncertainties, and Sensitivities. *J. Atmos. Sci.*, **60**, 607-625
- Kiladis, G. N. and K. M. Weickmann, 1992: Circulation Anomalies Associated with Tropical Convection during Northern Winter. *Mon. Wea. Rev.*, **120**, 1900-1923.

- Kiladis, G. N., K. H. Straub, and P. T. Haertel, 2005, Zonal and vertical structure of the Madden-Julian Oscillation. *J. Atmos. Sci.*, **62**, 2790-2809
- Knutson, T. R. and K. M. Weickmann, 1987: 30-60 Day Atmospheric Oscillations: Composite Life Cycles of Convection and Circulation Anomalies. *Mon. Wea. Rev.*, **115**, 1407-1436.
- Koster, R. D., M. J. Suarez, A. Ducharne, M. Stieglitz, and P. Kumar, 2000: A catchment-based approach to modeling land surface processes in a GCM. Part I: Model structure. *J. Geophys. Res.*, **105**, 24809–24822.
- Kummerow, C., J. Simpson, O. Thiele, W. Barnes, A. T. C. Chang, E. Stocker, R. F. Adler, A. Hou, R. Kakar, F. Wentz, P. Ashcroft, T. Kozu, Y. Hong, K. Okamoto, T. Iguchi, H. Kuroiwa, E. Im, Z. Haddad, G. Huffman, B. Ferrier, W. S. Olson, E. Zipser, E. A. Smith, T. T. Wilheit, G. North, T. Krishnamurti, and K. Nakamura, 2000: The status of the Tropical Rainfall Measuring Mission (TRMM) after two years in orbit. *J. Appl. Meteor.*, **39**, 1965-1982.
- Lau, N. C. and K. M. Lau, 1986: The Structure and Propagation of Intraseasonal Oscillations Appearing in a GFDL General Circulation Model. *J. Atmos. Sci.*, **43**, 2023-2047.
- Lau, W. K.-M. and D. E. Waliser, Eds., 2005: Intraseasonal Variability of the Atmosphere-Ocean Climate System, Springer, Heidelberg, Germany, 474.
- Lee, M. I., I. S. Kang, J. K. Kim, and B. E. Mapes, 2001: Influence of cloud-radiation interaction on simulating tropical intraseasonal oscillation with an atmospheric general circulation model. *J. Geophys. Res.*, **106**, 14219-14233.
- Lee, M. I., I. S. Kang, and B. E. Mapes, 2003: Impacts of cumulus convection parameterization on aqua-planet AGCM Simulations of tropical intraseasonal variability. *J. Meteor. Soc. Japan*, **81**, 963-992.
- Liebmann, B., H. H. Hendon, and J. D. Glick, 1994: The relationship between tropical

- cyclones of the western Pacific and Indian Oceans and the Madden-Julian oscillation. *J. Meteor. Soc. Japan*, **72**, 401-411.
- Liebmann, B. and C. A. Smith, 1996: Description of a complete (interpolated) outgoing longwave radiation dataset. *Bull. Amer. Meteor. Soc.*, **77**, 1275-1277.
- Lin, J., B. Mapes, M. Zhang, and M. Newman, 2004: Stratiform Precipitation, Vertical Heating Profiles, and the Madden-Julian Oscillation. *J. Atmos. Sci.*, **61**, 296-309.
- Lin, J. L., G. N. Kiladis, B. E. Mapes, K. M. Weickmann, K. R. Sperber, W. Lin, M. C. Wheeler, S. D. Schubert, A. Del Genio, L. J. Donner, S. Emori, J. F. Gueremy, F. Hourdin, P. J. Rasch, E. Roeckner, and J. F. Scinocca, 2006: Tropical intraseasonal variability in 14 IPCC AR4 climate models. Part I: Convective signals. *J. Climate*, **19**, 2665-2690.
- Lin, J. L., M. I. Lee, D. Kim, I. S. Kang, and D. M. W. Frierson, 2008: The Impacts of Convective Parameterization and Moisture Triggering on AGCM-Simulated Convectively Coupled Equatorial Waves. *J. Climate*, **21**, 883-909.
- Liu, P., B. Wang, K. R. Sperber, T. Li, and G. A. Meehl, 2005: MJO in the NCAR CAM2 with the Tiedtke Convective Scheme. *J. Climate*, **18**, 3007-3020.
- Lo, F. and H. H. Hendon, 2000: Empirical Extended-Range Prediction of the Madden-Julian Oscillation. *Mon. Wea. Rev.*, **128**, 2528-2543.
- Madden, R. A. and P. R. Julian, 1971: Detection of a 40-50 day oscillation in the zonal wind in the tropical Pacific. *J. Atmos. Sci.*, **28**, 702-708.
- , —, 1972: Description of Global-Scale Circulation Cells in the Tropics with a 40-50 Day Period. *J. Atmos. Sci.*, **29**, 1109-1123.
- , —, 1994: Observations of the 40-50-Day Tropical Oscillation - a Review. *Mon. Wea. Rev.*, **122**, 814-837.
- Maloney, E. D. and D. L. Hartmann, 1998: Frictional moisture convergence in a composite life cycle of the Madden-Julian oscillation. *J. Climate*, **11**, 2387-2403.

- ,—, 2000a: Modulation of hurricane activity in the Gulf of Mexico by the Madden-Julian oscillation. *Science*, **287**, 2002-2004.
- ,—, 2000b: Modulation of eastern North Pacific hurricanes by the Madden-Julian oscillation. *J. Climate*, **13**, 1451-1460.
- ,—, 2001: The sensitivity of intraseasonal variability in the NCAR CCM3 to changes in convective parameterization. *J. Climate*, **14**, 2015-2034.
- Maloney, E. D., 2002: An intraseasonal oscillation composite life cycle in the NCAR CCM3.6 with modified convection. *J. Climate*, **15**, 964-982.
- Marshall, A. G., O. Alves, and H. H. Hendon, 2008: An Enhanced Moisture Convergence-Evaporation Feedback Mechanism for MJO Air-Sea Interaction. *J. Atmos. Sci.*, **65**, 970-986.
- Matthews, A. J., B. J. Hoskins, J. M. Slingo, and M. Blackburn, 1996: Development of convection along the SPCZ within a Madden-Julian oscillation. *Quart. J. Roy. Meteor. Soc.*, **122**, 669-688.
- Miura, H., M. Satoh, T. Nasuno, A.T. Noda, and K. Oouchi, 2008: Madden-Julian Oscillation Event Realistically Simulated by a Global Cloud-Resolving Model. *Science*, **318**, 1763-1765. [DOI: 10.1126/science.1148443].
- Morita, J., Y. N. Takayabu, S. Shige and Y. Kodama, 2006: Analysis of rainfall characteristics of the Madden-Julian oscillation using TRMM satellite data. *Dynamics of Atmospheres and Oceans*, **42**, 107-126.
- Moorthi, S., and M. J. Suarez, 1992: Relaxed Arakawa-Schubert. A Parameterization of Moist Convection for General Circulation Models. *Mon. Wea. Rev.*, **120**, 978-1002
- Myers, D., and D. E. Waliser, 2003: Three dimensional water vapor and cloud variations associated with the Madden-Julian Oscillation during Northern Hemisphere winter. *J. Climate*, **16**, 929-950.
- Neale, R. B., J. H. Richter, M. Jochum, 2008: The impact of convection on ENSO:

- From a delayed oscillator to a series of events. *J. Climate*, **21**, 5094-5924
- Nordeng, T. E., 1994: Extended Versions of the Convective Parametrization Scheme at ECMWF and Their Impact on the Mean and Transient Activity of the Model in the Tropics. *European Centre for Medium-Range Weather Forecasts*.
- Numaguti, A., M. Takahashi, T. Nakajima, and A. Sumi, 1995: Development of an atmospheric general circulation model. *Climate System Dynamics and Modelling*, Vol. I-3, T. Matsuno, Ed., Center for Climate System Research, 1–27.
- Roeckner, E., K. Arpe, L. Bengtsson, M. Christoph, M. Claussen, L. Dumenil, M. Esch, M. Giorgetta, U. Schlese, and U. Schulzweida, 1996: The atmospheric general circulation model ECHAM-4: Model description and simulation of present-day climate. *MPI Report*, **218**, 90.
- Rui, H., and B. Wang, 1990: Development characteristics and dynamic structure of tropical intraseasonal convective anomalies. *J. Atmos. Sci.*, **47**, 357-379.
- Salby, M. L. and H. H. Hendon, 1994: Intraseasonal Behavior of Clouds, Temperature, and Motion in the Tropics. *J. Atmos. Sci.*, **51**, 2207-2224.
- Salby, M. L., R. R. Garcia, and H. H. Hendon, 1994: Planetary-Scale Circulations in the Presence of Climatological and Wave-Induced Heating. *J. Atmos. Sci.*, **51**, 2344-2367.
- Schumacher, C. and R. A. Houze Jr, 2003: Stratiform Rain in the Tropics as Seen by the TRMM Precipitation Radar. *J. Climate*, **16**, 1739-1756.
- Seo, K. H., J. K. E. Schemm, C. Jones, and S. Moorthi, 2005: Forecast skill of the tropical intraseasonal oscillation in the NCEP GFS dynamical extended range forecasts. *Climate Dyn.*, **25**, 265-284.
- Slingo, J. M., K. R. Sperber, J. S. Boyle, J. P. Ceron, M. Dix, B. Dugas, W. Ebisuzaki, J. Fyfe, D. Gregory, J. F. Gueremy, J. Hack, A. Harzallah, P. Inness, A. Kitoh, W. K. M. Lau, B. McAvaney, R. Madden, A. Matthews, T. N. Palmer, C. K. Park, D.

- Randall, and N. Renno, 1996: Intraseasonal oscillations in 15 atmospheric general circulation models: Results from an AMIP diagnostic subproject. *Climate Dyn.*, **12**, 325-357.
- Sperber, K. R., J. M. Slingo, and H. Annamalai, 2000: Predictability and the relationship between subseasonal and interannual variability during the Asian summer monsoon. *Quart. J. Roy. Meteor. Soc.*, **126**, 2545-2574.
- Sperber, K. R., 2003: Propagation and the vertical structure of the Madden-Julian oscillation. *Mon. Wea. Rev.*, **131**, 3018-3037.
- , 2004: Madden-Julian variability in NCAR CAM2.0 and CCSM2.0. *Climate Dyn.*, **23**, 259-278.
- Sperber, K. R., S. Gualdi, S. Legutke, and V. Gayler, 2005: The Madden-Julian oscillation in ECHAM4 coupled and uncoupled general circulation models. *Climate Dyn.*, **25**, 117-140.
- Sperber, K.R., and D. E. Waliser, 2008: New Approaches to Understanding, Simulating, and Forecasting the Madden-Julian Oscillation, Bulletin of the American Meteorology Society, DOI: 10.1175/2008BAMS2700.1.
- Sperber, K. R., H. Annamalai, 2008: Coupled model simulations of boreal summer intraseasonal (30–50 day) variability, Part 1: Systematic errors and caution on use of metrics. *Climate Dyn.*, **31**, 345-372
- Sperber, K. R., J. M. Slingo, D. E. Waliser, P. M. Inness, 2008: Coarse-Resolution Models Only Partly Cloudy, *Science*, **320**, 612-613, DOI: 10.1126/science.320.5876.612a.
- Takayabu, Y. N., T. Iguchi, M. Kachi, A. Shibata, and H. Kanzawa, 1999: Abrupt termination of the 1997-98 El Nino in response to a Madden-Julian oscillation. *Nature*, **402**, 279-282.
- Thayer-Calder, K., 2008: The role of moisture in the MJO: a comparison of tropical

convection processes in the CAM and super-parameterized CAM. M. S. Thesis, Colorado State University, Dept. of Atmospheric Science, Fort Collins, CO USA, 74pp.

Thayer-Calder, K. and D. A. Randall, 2009: The role of convective moistening in the formation and progression of the MJO. *J. Atmos. Sci.* (in preparation)

Tian, B. J., D. E. Waliser, E. Fetzer, B. Lambrigtsen, Y. Yung, and B. Wang, 2006: Vertical Moist Thermodynamic Structure and Spatial-temporal Evolution of the Madden-Julian Oscillation in Atmospheric Infrared Sounder Observations. *J. Atmos. Sci.*, **63**, 2462-2485.

Tiedtke, M., 1989: A Comprehensive Mass Flux Scheme for Cumulus Parameterization in Large-Scale Models. *Mon. Wea. Rev.*, **117**, 1779-1800.

Tokioka, T., K. Yamazaki, A. Kitoh, and T. Ose, 1988: The equatorial 30-60 day oscillation and the Arakawa-Schubert penetrative cumulus parameterization. *J. Meteor. Soc. Japan*, **66**, 883-901.

Uppala, S. M., P. W. Kallberg, A. J. Simmons, U. Andrae, V. D. Bechtold, M. Fiorino, J. K. Gibson, J. Haseler, A. Hernandez, G. A. Kelly, X. Li, K. Onogi, S. Saarinen, N. Sokka, R. P. Allan, E. Andersson, K. Arpe, M. A. Balmaseda, A. C. M. Beljaars, L. Van De Berg, J. Bidlot, N. Bormann, S. Caires, F. Chevallier, A. Dethof, M. Dragosavac, M. Fisher, M. Fuentes, S. Hagemann, E. Holm, B. J. Hoskins, L. Isaksen, P. Janssen, R. Jenne, A. P. McNally, J. F. Mahfouf, J. J. Morcrette, N. A. Rayner, R. W. Saunders, P. Simon, A. Sterl, K. E. Trenberth, A. Untch, D. Vasiljevic, P. Viterbo, and J. Woollen, 2005: The ERA-40 re-analysis. *Quart. J. Roy. Meteor. Soc.*, **131**, 2961-3012.

Vitart, F., S. Woolnough, M. A. Balmaseda, and A. M. Tompkins, 2007: Monthly Forecast of the Madden-Julian Oscillation Using a Coupled GCM. *Mon. Wea. Rev.*, **135**, 2700-2715.

- Waliser, D. E., 2006: Intraseasonal Variability. *The Asian Monsoon*, B. Wang, Ed., Springer, Heidelberg, Germany, 844
- Waliser, D. E., K. M. Lau, and J. H. Kim, 1999: The influence of coupled sea surface temperatures on the Madden-Julian oscillation: A model perturbation experiment. *J. Atmos. Sci.*, **56**, 333-358.
- Waliser, D. E., K. Jin, I. S. Kang, W. F. Stern, S. D. Schubert, M. L. C. Wu, K. M. Lau, M. I. Lee, V. Krishnamurthy, A. Kitoh, G. A. Meehl, V. Y. Galin, V. Satyan, S. K. Mandke, G. Wu, Y. Liu, and C. K. Park, 2003: AGCM simulations of intraseasonal variability associated with the Asian summer monsoon. *Climate Dyn.*, **21**, 423-446.
- Waliser, D. E., 2006: Predictability of Tropical Intraseasonal Variability. *Predictability of Weather and Climate*, T. Palmer and R. Hegedorn, Eds., Cambridge University Press, 718pp
- Wang, B., 1988: Dynamics of Tropical Low-Frequency Waves: An Analysis of the Moist Kelvin Wave. *J. Atmos. Sci.*, **45**, 2051-2065.
- Wang, W. Q. and M. E. Schlesinger, 1999: The dependence on convection parameterization of the tropical intraseasonal oscillation simulated by the UIUC 11-layer atmospheric GCM. *J. Climate*, **12**, 1423-1457.
- Wang, W. Q., S. Saha, H. L. Pan, S. Nadiga, G. White, 2005, Simulation of ENSO in the New NCEP Coupled Forecast System Model (CFS03). *Mon. Wea. Rev.*, **133**, 1574-1593
- Weickmann, K. M., G. R. Lussky, and J. E. Kutzbach, 1985: Intraseasonal (30-60 Day) Fluctuations of Outgoing Longwave Radiation and 250 mb Streamfunction during Northern Winter. *Mon. Wea. Rev.*, **113**, 941-961.
- Wheeler, M. and G. N. Kiladis, 1999: Convectively coupled equatorial waves: Analysis of clouds and temperature in the wavenumber-frequency domain. *J. Atmos. Sci.*, **56**, 374-399.

- Wheeler, M. and K. M. Weickmann, 2001: Real-Time Monitoring and Prediction of Modes of Coherent Synoptic to Intraseasonal Tropical Variability. *Mon. Wea. Rev.*, **129**, 2677-2694.
- Wheeler, M. C. and H. H. Hendon, 2004: An All-Season Real-Time Multivariate MJO Index: Development of an Index for Monitoring and Prediction. *Mon. Wea. Rev.*, **132**, 1917-1932.
- Wheeler, M. C. and J. L. McBride, 2005: Australian-Indonesian monsoon. *Intraseasonal Variability in the Atmosphere-Ocean Climate System*, W. K. M. Lau and D. E. Waliser, Eds., Springer, Heidelberg, Germany, 125-173.
- Xie, P. P. and P. A. Arkin, 1997: Global precipitation: A 17-year monthly analysis based on gauge observations, satellite estimates, and numerical model outputs. *Bull. Amer. Meteor. Soc.*, **78**, 2539-2558.
- Yasunari, T., 1979: Cloudiness fluctuations associated with the Northern Hemisphere summer monsoon. *J. Met. Soc. Japan*, **57**, 227-242.
- Yu, L., and R. A. Weller, 2007: Objectively analyzed air-sea heat fluxes for the global ice-free oceans. *Bull. Amer. Meteor. Soc.*, **88**, 527-539.
- Zhang, C., 2005: The Madden Julian Oscillation. *Reviews of Geophysics*, **43**, RG2003, doi:10.1029/2004RG000158.
- Zhang, C., M. Dong, H. H. Hendon, E. D. Maloney, A. Marshall, K. R. Sperber, and W. Wang, 2006: Simulations of the Madden-Julian Oscillation in Four Pairs of Coupled and Uncoupled Global Models. *Climate Dyn.*, DOI: 10.1007/s00382-006-0148-2.
- Zhang, G. J. and N.A. McFarlane, 1995: Sensitivity of climate simulations to the parameterization of cumulus convection in the Canadian Climate Centre general circulation model. *Atmosphere-Ocean*, **33**, 407-446.
- Zhang, G. J. and M. Mu, 2005a: Simulation of the Madden-Julian Oscillation in the

NCAR CCM3 Using a Revised Zhang-McFarlane Convection Parameterization Scheme. *J. Climate*, **18**, 4046-4064.

Zhang, G. J., and M. Mu, 2005b: Effects of modifications to the Zhang-McFarlane convection parameterization on the simulation of the tropical precipitation in the National Center for Atmospheric Research Community Climate Model, version 3. *J. Geophys. Res.*, **110**, D09109, doi:10.1029/2004JD005617.

Table 1. Descriptions of participating models

Model	Horizontal Resolution	Vertical Resolution (top level)	Cumulus parameterization	Integration	Reference
CAM3.5 - NCAR	1.9° lat x 2.5° lon	26 (2.2hPa)	Mass flux (Zhang and McFarlane 1995, with entrainment-based closure)	20 years 01JAN1986-31DEC2005	Neale et al. (2008)
CAM3z - SIO	T42(2.8°)	26 (2.2hPa)	Mass flux (Zhang and McFarlane 1995, with free tropospheric quasi-equilibrium closure)	15 years 29JAN1980-23JUL1995	Zhang and Mu (2005b)
CFS - NCEP	T62(1.8°)	64 (0.2hPa)	Mass flux (Hong and Pan 1998)	20 years	Wang et al. (2005)
CM2.1 - GFDL	2° lat x 2.5° lon	24 (4.5hPa)	Mass flux (RAS; Moorthi and Suarez 1992)	20 years	Delworth et al. (2006)
ECHAM4 /OPYC* - MPI	T42(2.8°)	19 (10hPa)	Mass flux (Tiedtke 1989, adjustment closure Nordeng 1994)	20 years	Roeckner et al. (1996), Sperber et al. (2005)
GEOS5 - NASA	1° lat x 1.25° lon	72 (0.01hPa)	Mass flux (RAS; Moorthi and Suarez 1992)	12 years 01DEC1993-30NOV2005	To be documented
SNU - SNU	T42(2.8°)	20 (10hPa)	Mass flux (Numaguti et al. 1995)	20 years 01JAN1986-31DEC2005	Lee et al. (2003)
SPCAM - CSU	T42(2.8°)	26 (3.5hPa)	Superparameterization (Khairoutdinov and Randall 2003)	19 years 01OCT1985-25SEP2005	Khairoutdinov et al. (2005)

Table 2. Average of e-folding time scale over all initial phases

Observation/Models	e-folding day
Observation	31.2
CAM3.5	20.5
CAM3z	21.5
CFS	24.9
CM2.1	20.7
ECHAM4/OPYC	28.9
GEOS	20.7
SNU	22.8
SPCAM	24.5
Model average	23.0

Figure Captions

Figure 1. November-April mean precipitation (shaded) and 850hPa zonal wind (contoured) of a) CMAP/NCEP/NCAR, b) CAM3.5, c) CAM3z, d) CFS, e) CM2.1, f) ECHAM4/OPYC, g) GEOS5, h) SNU, and i) SPCAM. Contours of mean 850hPa zonal wind are plotted every 3 ms^{-1} , with the zero line represented by a thick solid line. The unit is mmday^{-1} for precipitation and ms^{-1} for 850hPa zonal wind.

Figure 2. Scatter plot of pattern correlation and normalized RMSE for November-April mean a) precipitation b) 850hPa zonal wind, d) outgoing longwave radiation, e) 200hPa zonal wind, and for 20-100 day filtered variance map of c) precipitation and f) 850hPa zonal wind. The region for pattern correlation and normalized RMSE is 40°E - 220°E , 25°S - 15°N . RMSE is normalized by standard deviation of the observed value.

Figure 3. As in Figure 1, except for variance of 20-100 day band pass filtered precipitation and 850hPa zonal wind. Contours of 850hPa zonal wind variance are plotted every $3 \text{ m}^2 \text{ s}^{-2}$, with the $9 \text{ m}^2 \text{ s}^{-2}$ line represented by the thick solid line. The unit is $\text{mm}^2 \text{ day}^{-2}$ for precipitation and $\text{m}^2 \text{ s}^{-2}$ for zonal wind.

Figure 4. November-April wavenumber-frequency spectra of 10°N - 10°S averaged precipitation (shaded) and 850hPa zonal wind (contoured). a) CMAP/NCEP/NCAR, b) CAM3.5, c) CAM3z, d) CFS, e) CM2.1, f) ECHAM4/OPYC, g) GEOS5, h) SNU, and i) SPCAM. Individual November-April spectra were calculated for each year, and then averaged over all years of data. Only the climatological seasonal cycle and

time mean for each November-April segment were removed before calculation of the spectra. Units for the precipitation (zonal wind) spectrum are $\text{mm}^2 \text{ day}^{-2}$ ($\text{m}^2 \text{ s}^{-2}$) per frequency interval per wavenumber interval. The bandwidth is $(180 \text{ d})^{-1}$.

Figure 5. Scatter plot of east/west ratio of power based on the data in Fig. 4. The east/west ratio is calculated by dividing the sum of eastward propagating power by westward propagating counterpart within wavenumber 1-3 (1-2 for zonal wind), period 30-80 days.

Figure 6. First two CEOF modes of 20-100 day 15°S - 15°N averaged 850hPa and 200hPa zonal wind and OLR. a) NCEP/NCAR and AVHRR, b) CAM3.5, c) CAM3z, d) CFS, e) CM2.1, f) ECHAM4/OPYC, g) GEOS5, h) SNU, and i) SPCAM. The total variance explained by each mode is shown in the lower-left of each panel. The coherence squared between principle components of two modes within 30-80 day period is given above the upper panel. Sign and location (upper or lower) of each mode are arbitrarily adjusted to be similar to observation. The mode which has largest percentage variance explained is the first mode.

Figure 7. The power spectrum of the unfiltered PC derived by projecting the CEOF's onto unfiltered data (seasonal cycle removed; Blue: 1st mode, Green: 2nd mode). Dashed lines show the 99% confidence limit for a red noise spectrum.

Figure 8. PC1 and PC2 phase space composite curves of the MJO index from the CEOF analysis. The PC's have each been normalized by their respective standard deviations. For each initial phase, strong cases are selected when the MJO amplitude $(\text{PC1}^2 + \text{PC2}^2)^{1/2}$ exceeded 1.5 . Then data for each of the next 40 days from initial day

are averaged over all strong cases to show the evolution of the MJO index. (Blue: from odd number initial phase, Green: from even number initial phase).

Figure 9. Phase-longitude diagram of OLR (contour, plotted every 5 Wm^{-2} , green-positive/purple-negative) and surface latent heat flux (Wm^{-2} ; shaded). Phases are from MJO life-cycle composite and values are 5°S - 5°N averaged.

Figure 10. Same as Fig. 9, except for 925hPa moisture convergence. The unit of convergence is $\text{kg kg}^{-1} \text{ s}^{-1}$.

Figure 11. Pressure-phase diagram of specific humidity anomalies (shaded) at three different longitudes 80°E (left), 130°E (middle) 140°W (right) averaged between 5°S - 5°N . Phases are defined as in Fig. 10. The units for specific humidity are g kg^{-1} . OLR anomalies are plotted in lower panel (Wm^{-2}).

Figure 12. Scatter plot of pattern correlation and mean coherence squared for November-April mean a) precipitation, b) 850hPa zonal wind, c) outgoing longwave radiation, and d) 200hPa zonal wind. The region for the pattern correlation calculation is 40°E - 220°E , 25°S - 15°N . Mean coherence squared is calculated between two leading PC's from CEOF analysis (30-80 day period). The value in the parentheses is the correlation between the two variables.

Figure 13. Composite vertical profile of relative humidity based on precipitation rate a) ERA40/GPCP, b) CAM3.5, c) CAM3z, d) CM2.1, e) ECHAM4/OPYC, f) SNU, and g) SNU without convective inhibition function. The precipitation rate is plotted on a

log scale) with the relative humidity averaged for each bin shown on the x-axis. The data is analyzed over 40°E-220°E, 10°S-10°N.

Figure 14. November-April mean stratiform rain fraction of a) TRMM 3A25 product, b) CAM3.5, c) CAM3z, d) ECHAM4/OPYC, e) SNU and f) SNU (no trigger). Areas with November-April mean rain of less than 2mm day⁻¹ are not included.

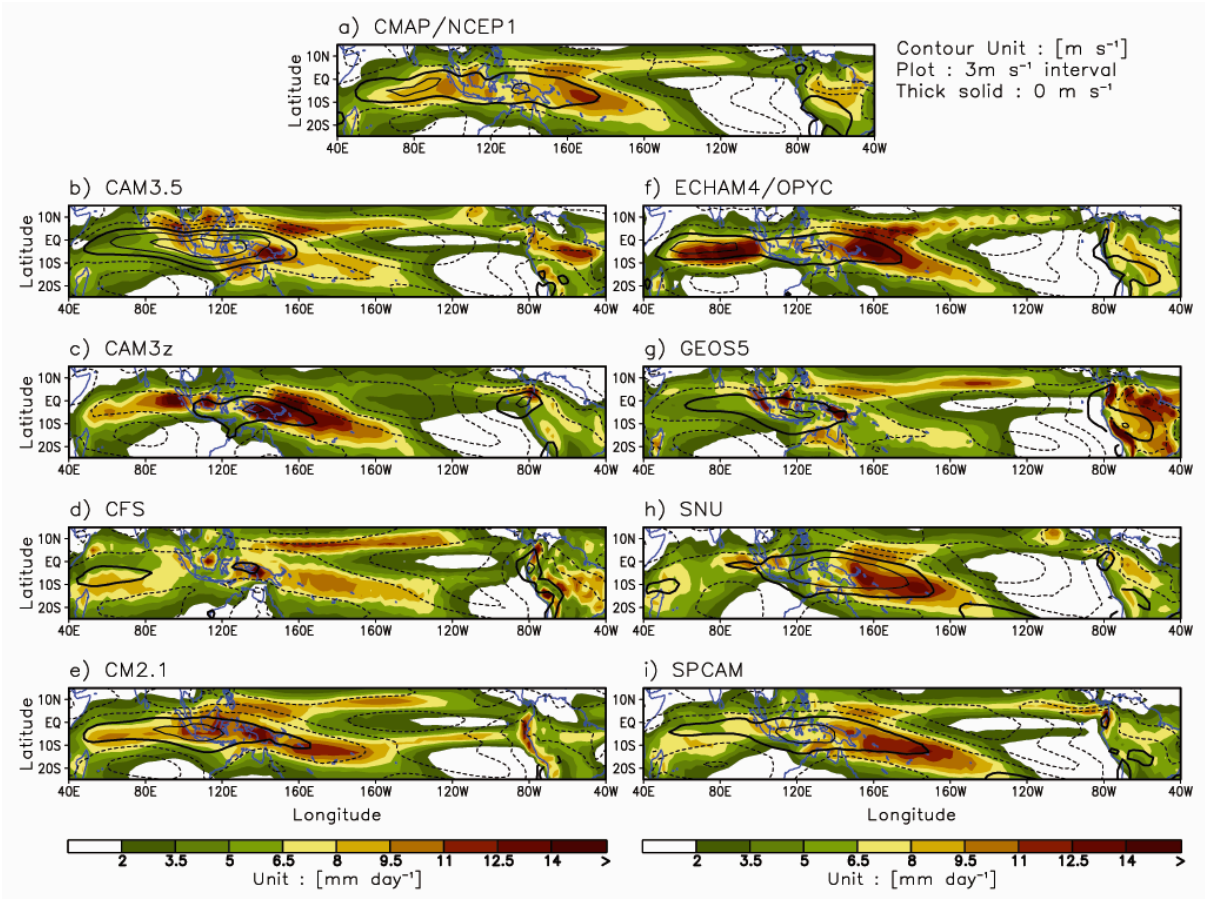


Figure 1. November-April mean precipitation (shaded) and 850hPa zonal wind (contoured) of a) CMAP/NCEP/NCAR, b) CAM3.5, c) CAM3z, d) CFS, e) CM2.1, f) ECHAM4/OPYC, g) GEOS5, h) SNU, and i) SPCAM. Contours of mean 850hPa zonal wind are plotted every 3 m s^{-1} , with the zero line represented by a thick solid line. The unit is mm day^{-1} for precipitation and m s^{-1} for 850hPa zonal wind.

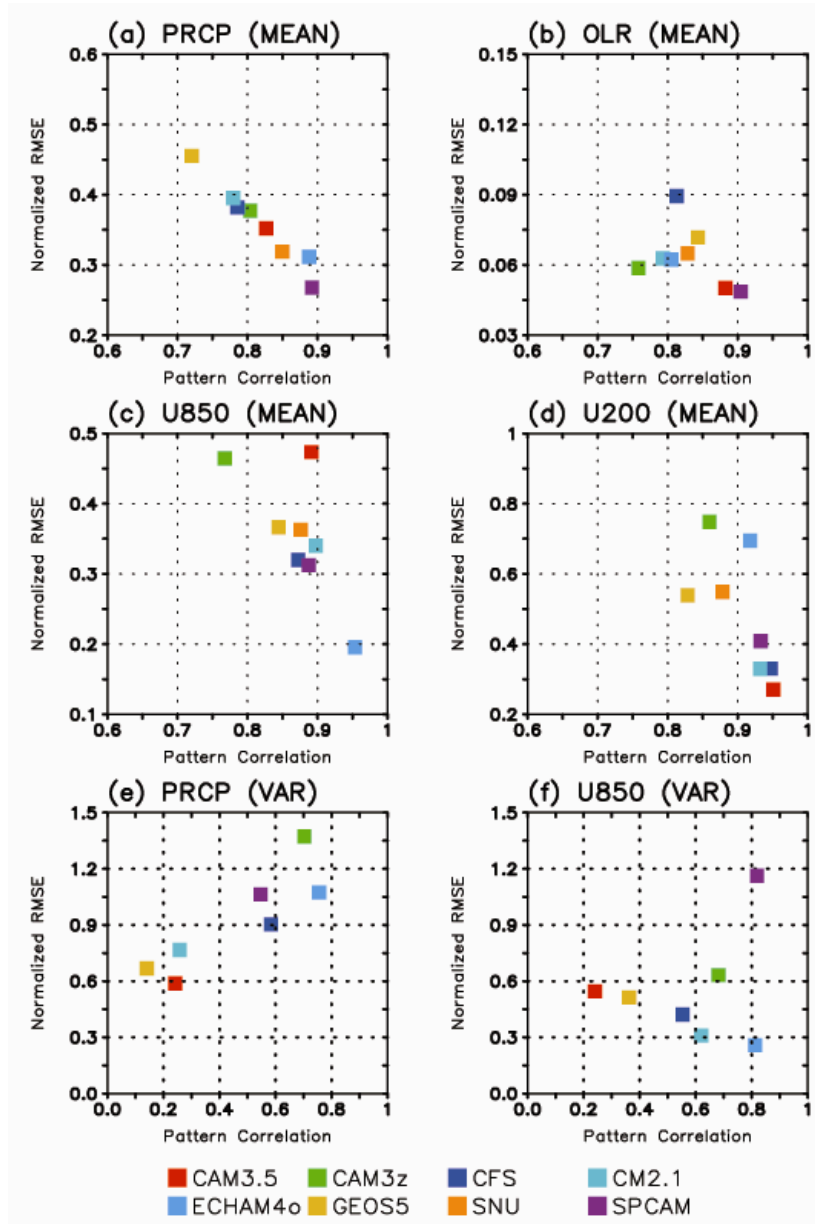


Figure 2. Scatter plot of pattern correlation and normalized RMSE for November-April mean a) precipitation b) 850hPa zonal wind, d) outgoing longwave radiation, e) 200hPa zonal wind, and for 20-100 day filtered variance map of c) precipitation and f) 850hPa zonal wind. The region for pattern correlation and normalized RMSE is 40°E-220°E, 25°S-15°N. RMSE is normalized by standard deviation of the observed value.

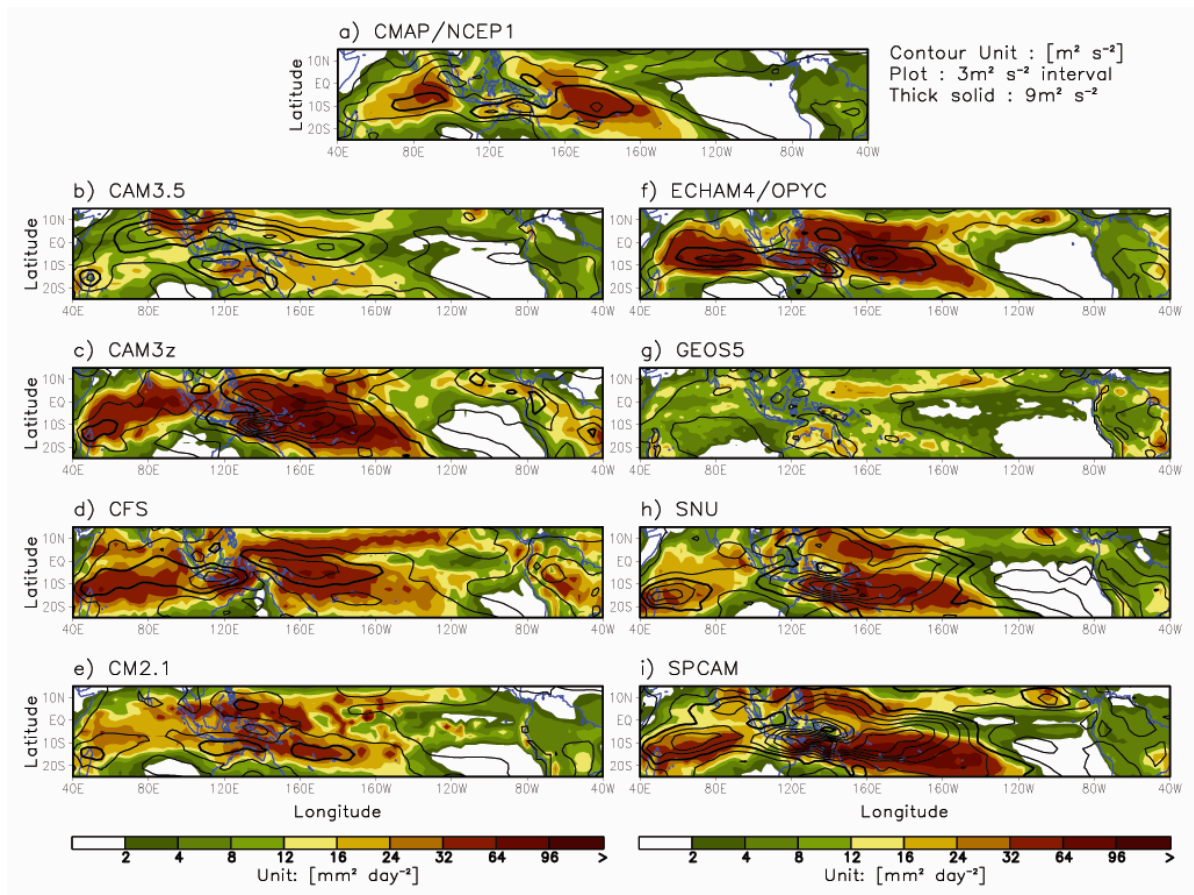


Figure 3. As in Figure 1, except for variance of 20-100 day band pass filtered precipitation and 850hPa zonal wind. Contours of 850hPa zonal wind variance are plotted every $3 \text{ m}^2 \text{ s}^{-2}$, with the $9 \text{ m}^2 \text{ s}^{-2}$ line represented by the thick solid line. The unit is $\text{mm}^2 \text{ day}^{-2}$ for precipitation and $\text{m}^2 \text{ s}^{-2}$ for zonal wind.

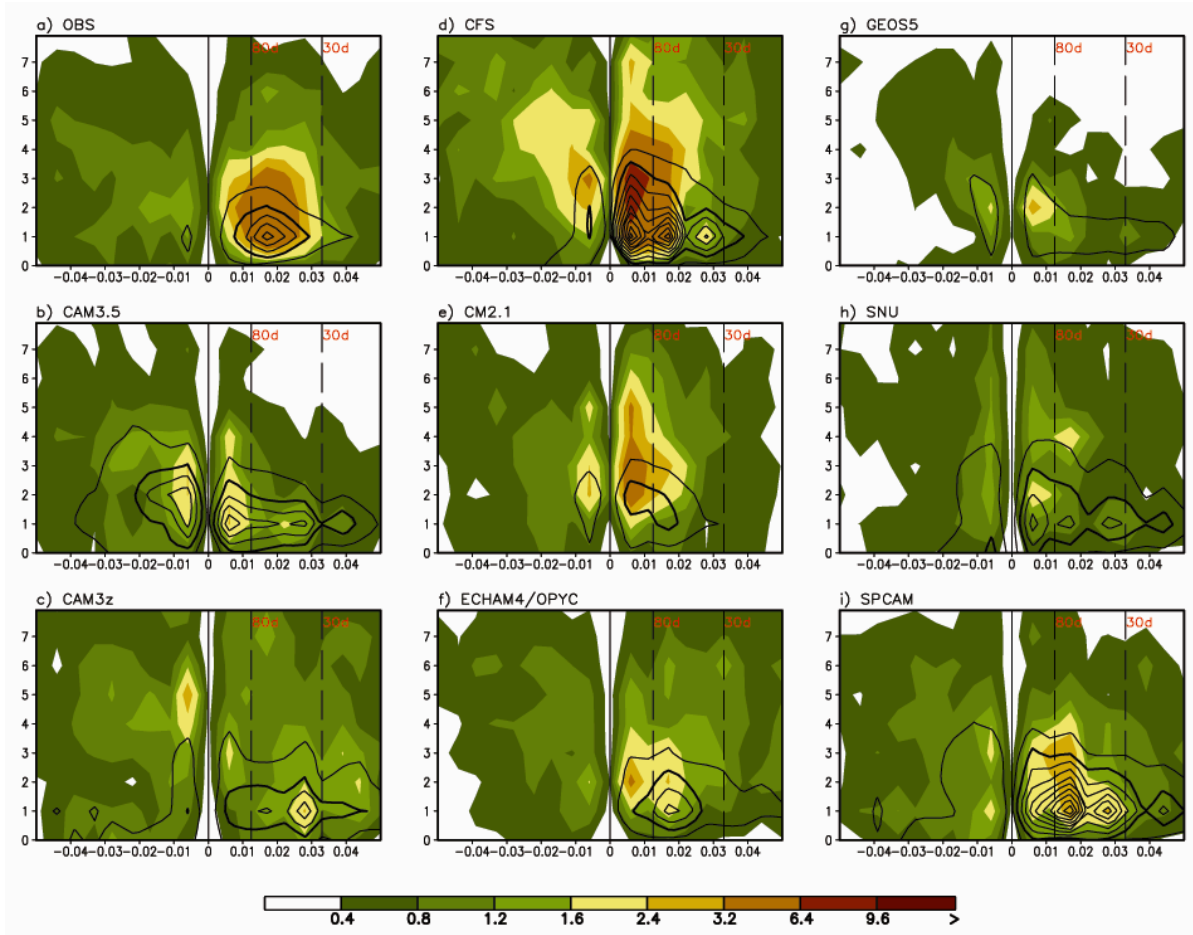


Figure 4. November-April wavenumber-frequency spectra of 10°N - 10°S averaged precipitation (shaded) and 850hPa zonal wind (contoured). a) CMAP/NCEP/NCAR, b) CAM3.5, c) CAM3z, d) CFS, e) CM2.1, f) ECHAM4/OPYC, g) GEOS5, h) SNU, and i) SPCAM. Individual November-April spectra were calculated for each year, and then averaged over all years of data. Only the climatological seasonal cycle and time mean for each November-April segment were removed before calculation of the spectra. Units for the precipitation (zonal wind) spectrum are $\text{mm}^2 \text{day}^{-2}$ ($\text{m}^2 \text{s}^{-2}$) per frequency interval per wavenumber interval. The bandwidth is $(180 \text{ d})^{-1}$.

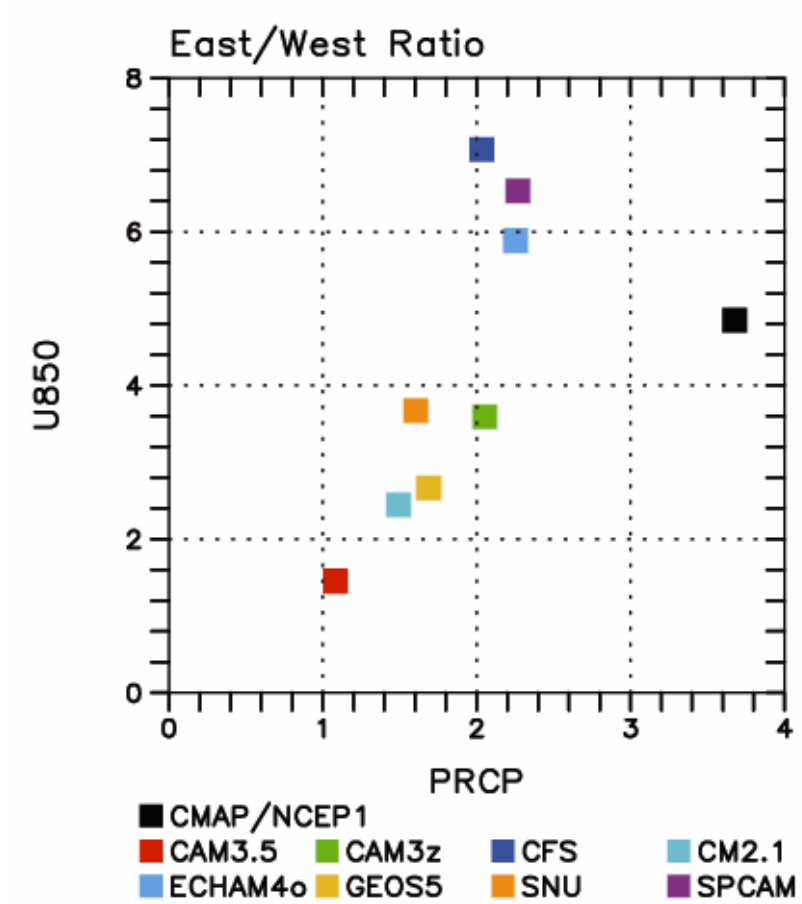


Figure 5. Scatter plot of east/west ratio of power based on the data in Fig. 4. The east/west ratio is calculated by dividing the sum of eastward propagating power by westward propagating counterpart within wavenumber 1-3 (1-2 for zonal wind), period 30-80 days.

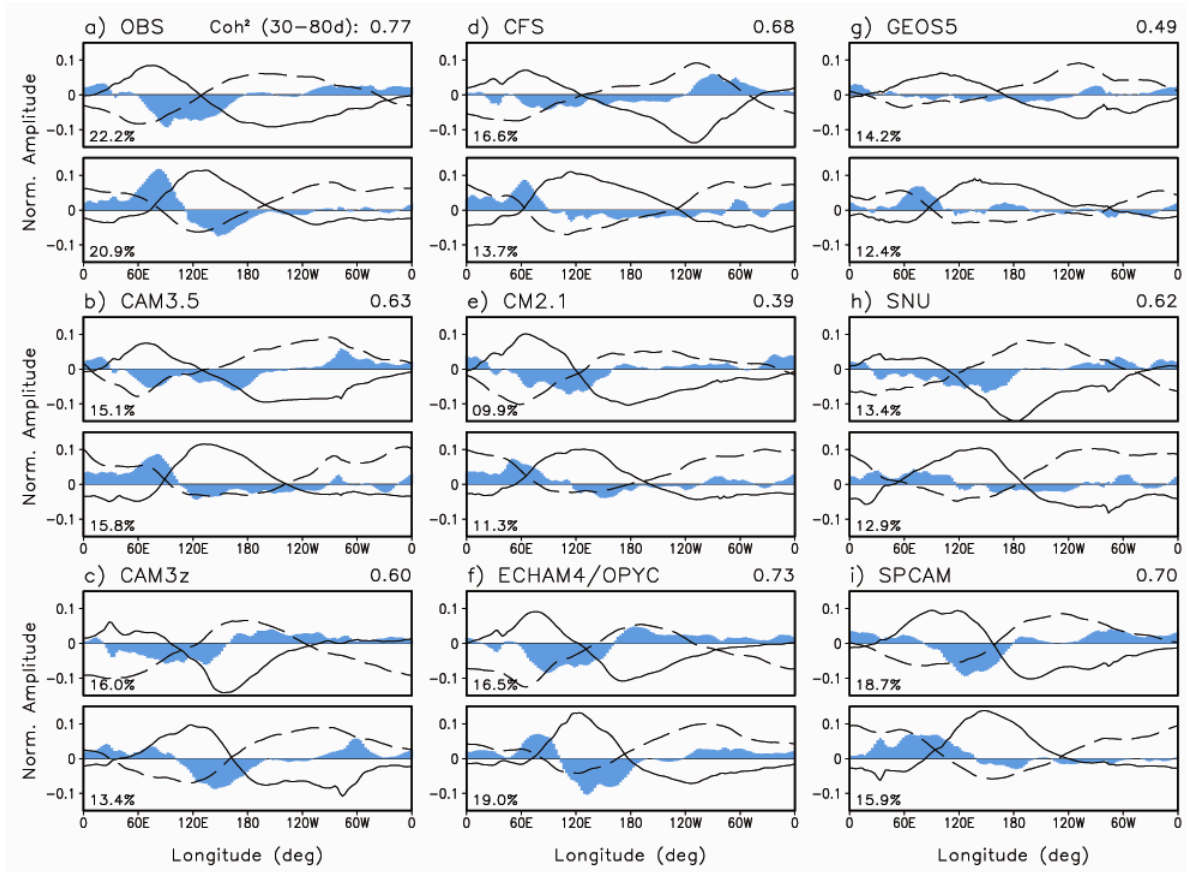


Figure 6. First two CEOF modes of 20-100 day 15°S-15°N averaged 850hPa and 200hPa zonal wind and OLR. a) NCEP/NCAR and AVHRR, b) CAM3.5, c) CAM3z, d) CFS, e) CM2.1, f) ECHAM4/OPYC, g) GEOS5, h) SNU, and i) SPCAM. The total variance explained by each mode is shown in the lower-left of each panel. The coherence squared between principle components of two modes within 30-80 day period is given above the upper panel. Sign and location (upper or lower) of each mode are arbitrarily adjusted to be similar to observation. The mode which has largest percentage variance explained is the first mode.

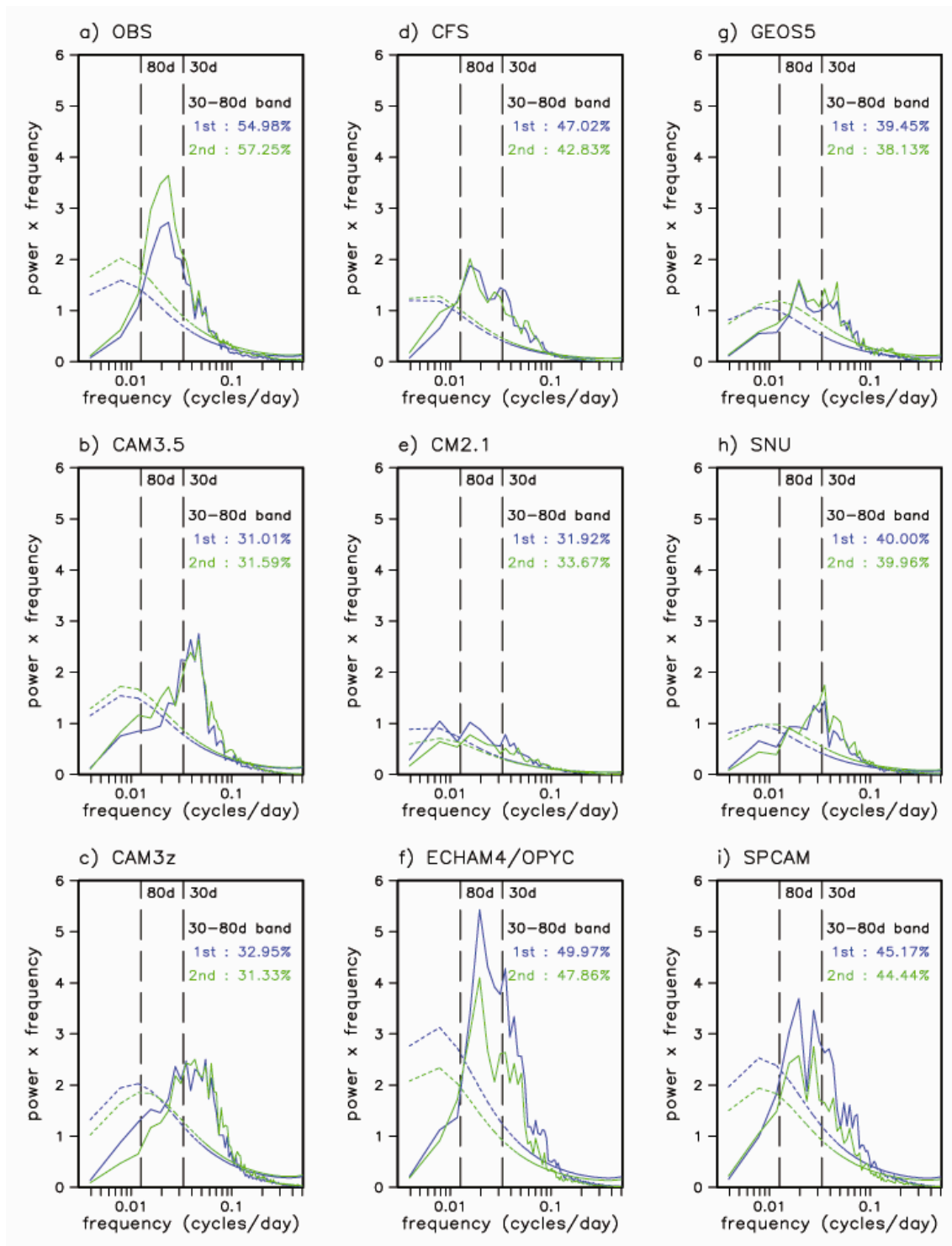


Figure 7. The power spectrum of the unfiltered PC derived by projecting the CEOF's onto unfiltered data (seasonal cycle removed; Blue: 1st mode, Green: 2nd mode). Dashed lines show the 99% confidence limit for a red noise spectrum.

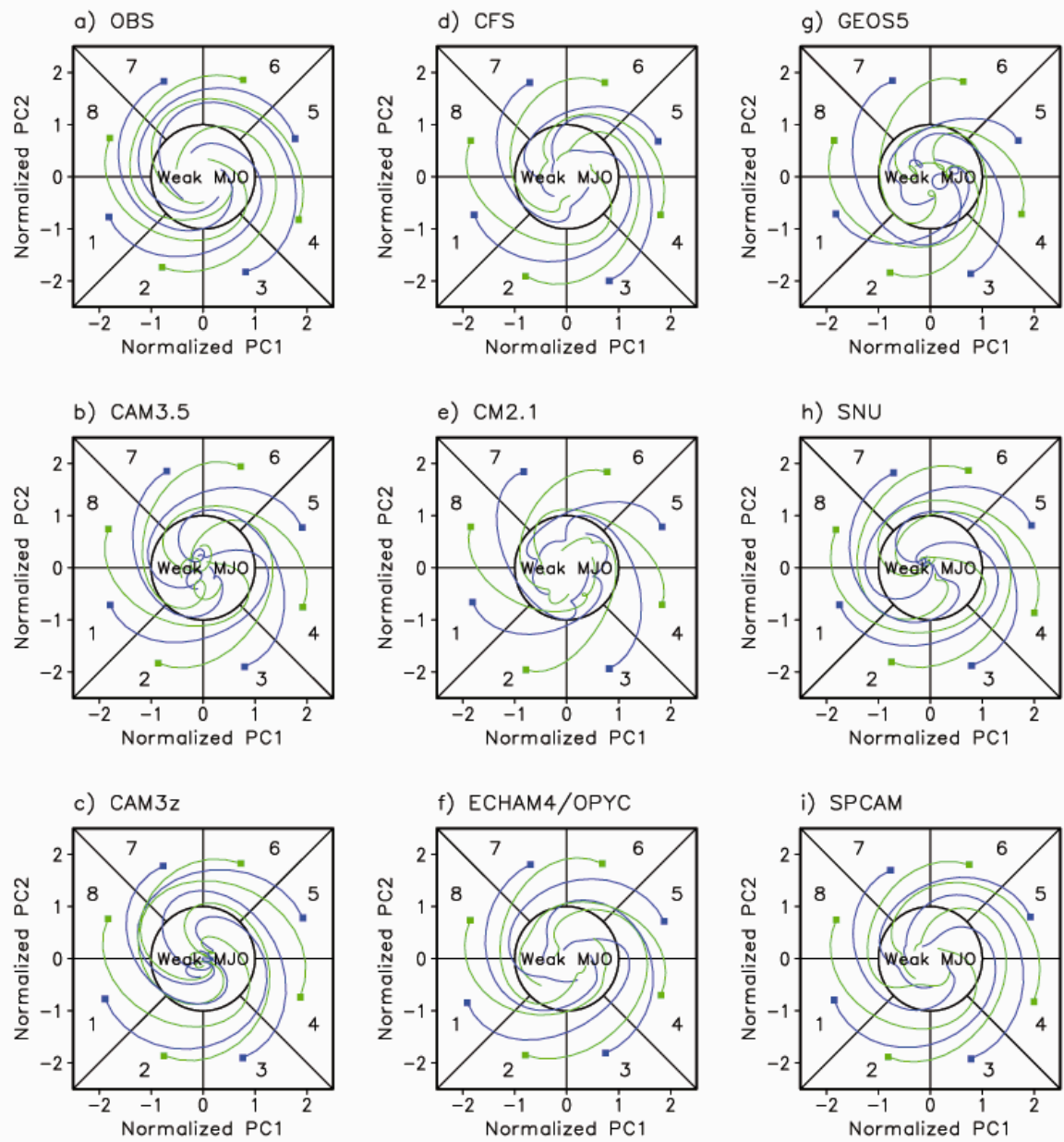


Figure 8. PC1 and PC2 phase space composite curves of the MJO index from the CEOF analysis. The PC's have each been normalized by their respective standard deviations. For each initial phase, strong cases are selected when the MJO amplitude $(PC1^2+PC2^2)^{1/2}$ exceeded 1.5. Then data for each of the next 40 days from initial day are averaged over all strong cases to show the evolution of the MJO index. (Blue: from odd number initial phase, Green: from even number initial phase).

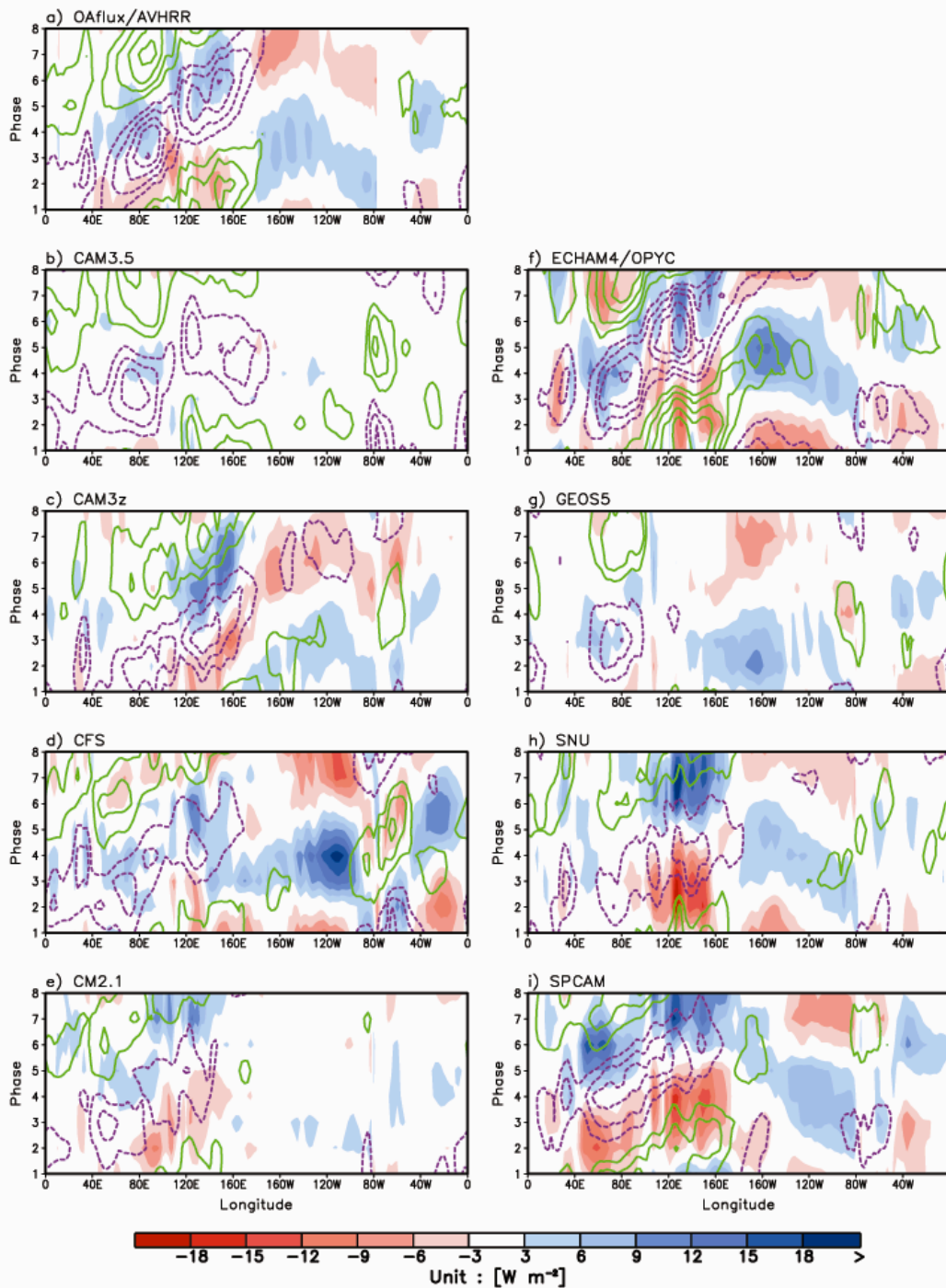


Figure 9. Phase-longitude diagram of OLR (contour, plotted every 5 W m^{-2} , green-positive/ purple-negative) and surface latent heat flux (W m^{-2} ; shaded). Phases are from MJO life-cycle composite and values are 5°S - 5°N averaged.

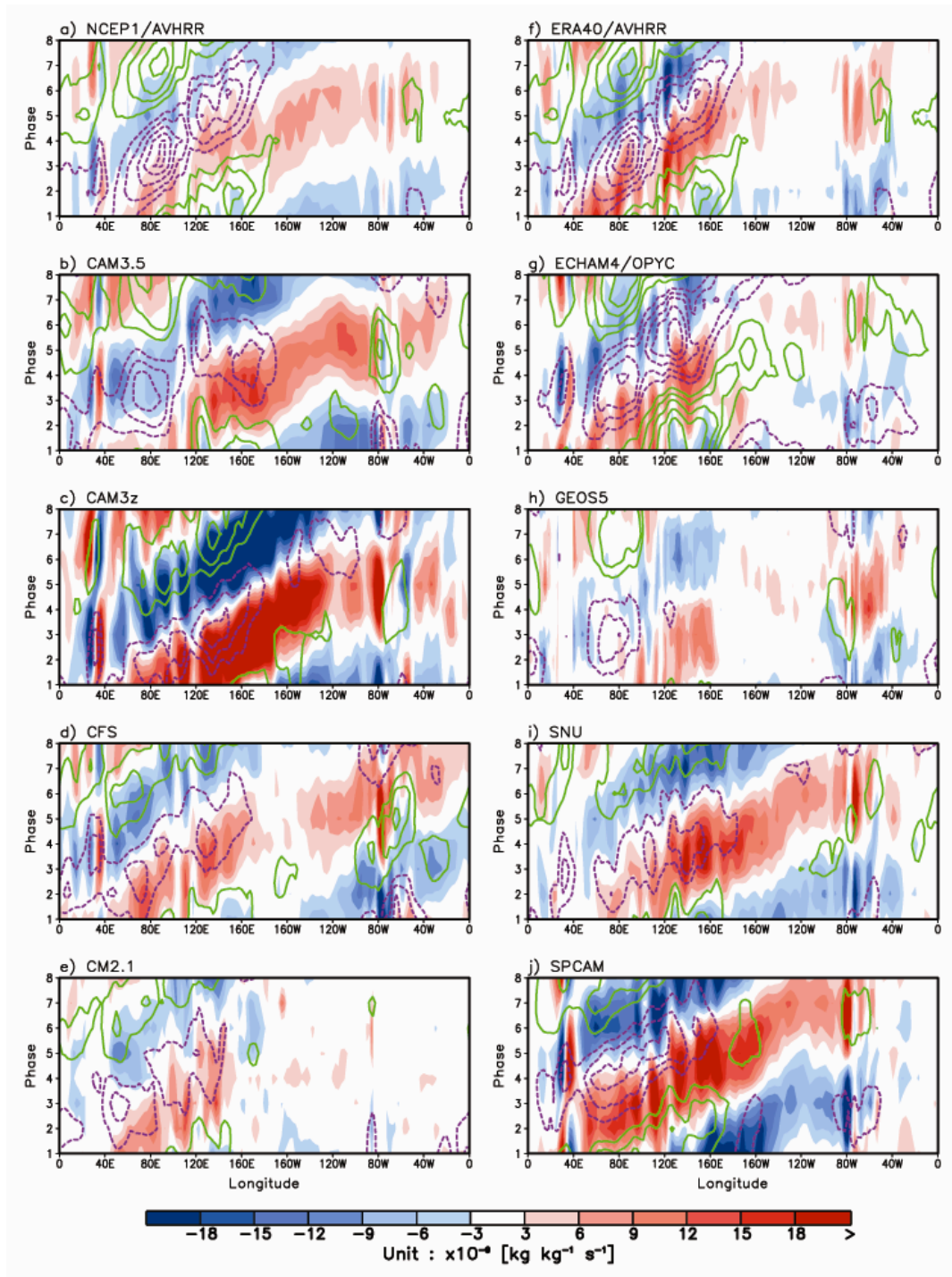


Figure 10. Same as Fig. 9, except for 925hPa moisture convergence. The unit of convergence is $\text{kg kg}^{-1} \text{ s}^{-1}$.

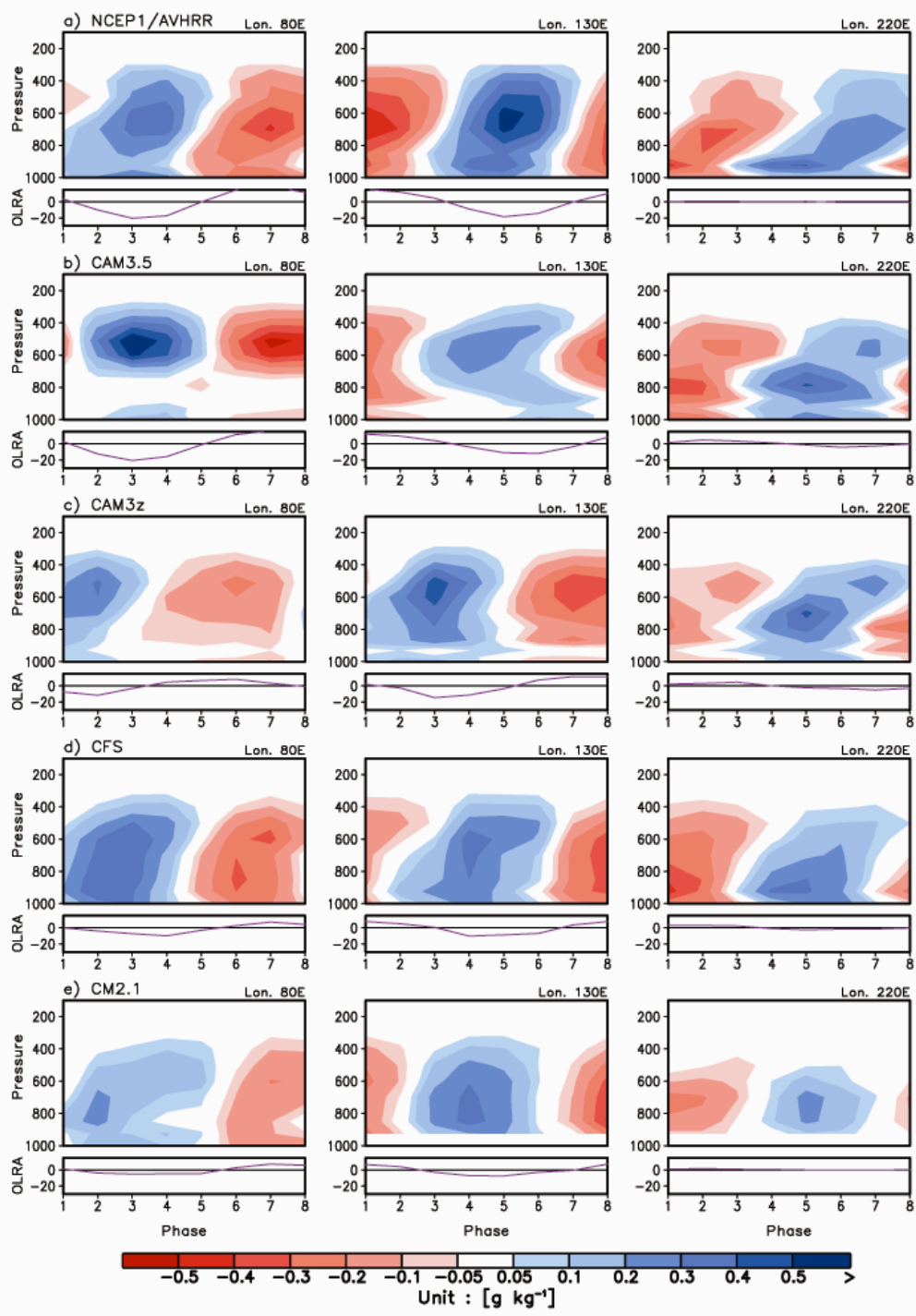


Figure 11. Pressure-phase diagram of specific humidity anomalies (shaded) at three different longitudes 80°E (left), 130°E (middle) 140°W (right) averaged between 5°S-5°N. Phases are defined as in Fig. 10. The units for specific humidity are g kg⁻¹. OLR anomalies are plotted in lower panel (Wm⁻²).

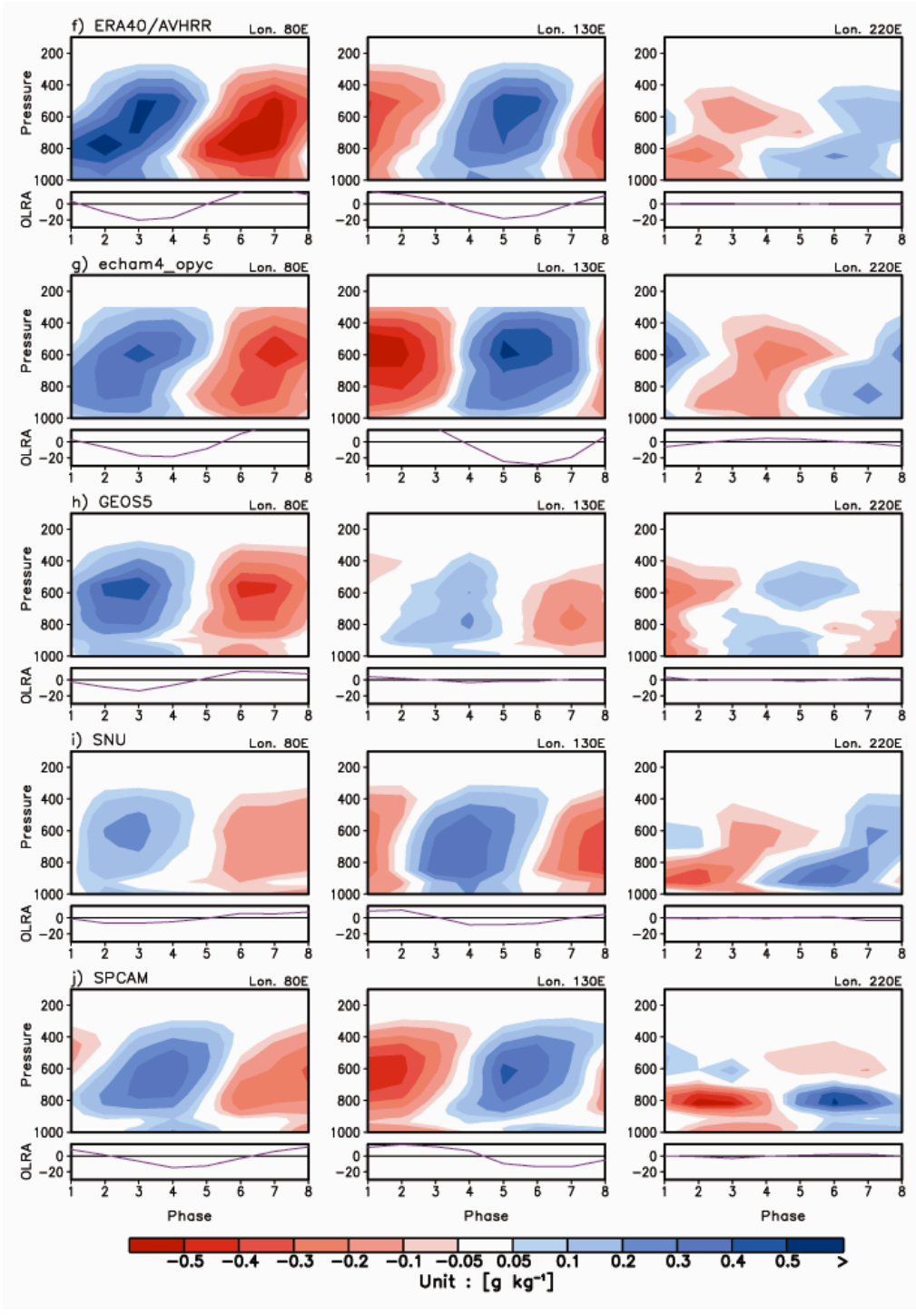


Figure 11. (continued)

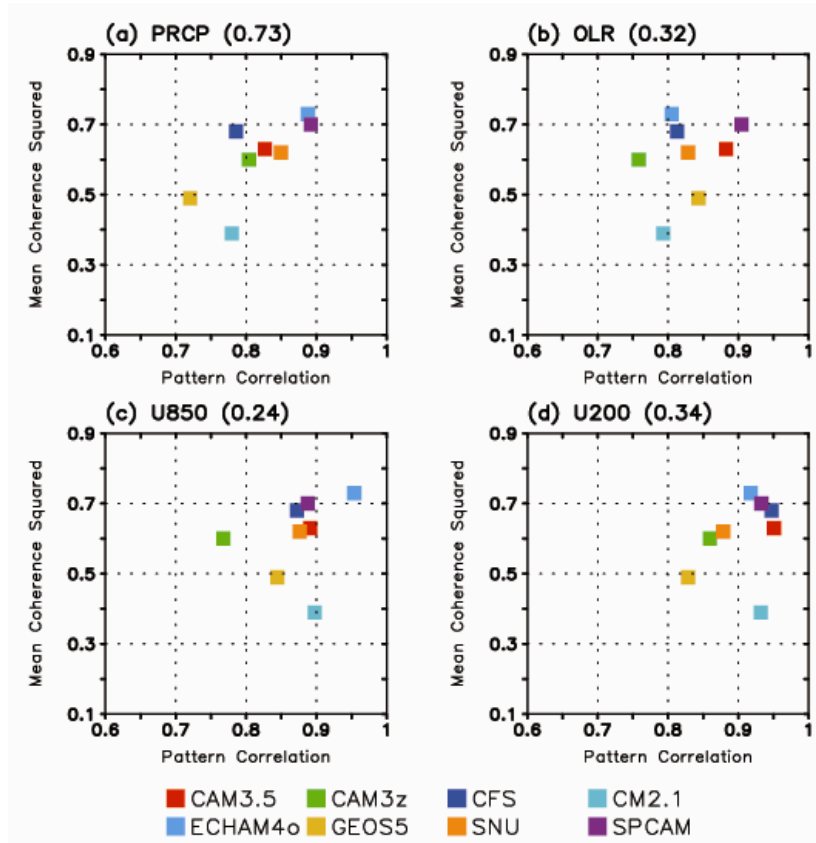


Figure 12. Scatter plot of pattern correlation and mean coherence squared for November-April mean a) precipitation, b) 850hPa zonal wind, c) outgoing longwave radiation, and d) 200hPa zonal wind. The region for the pattern correlation calculation is 40°E-220°E, 25°S-15°N. Mean coherence squared is calculated between two leading PC's from CEOF analysis (30-80 day period). The value in the parentheses is the correlation between the two variables.

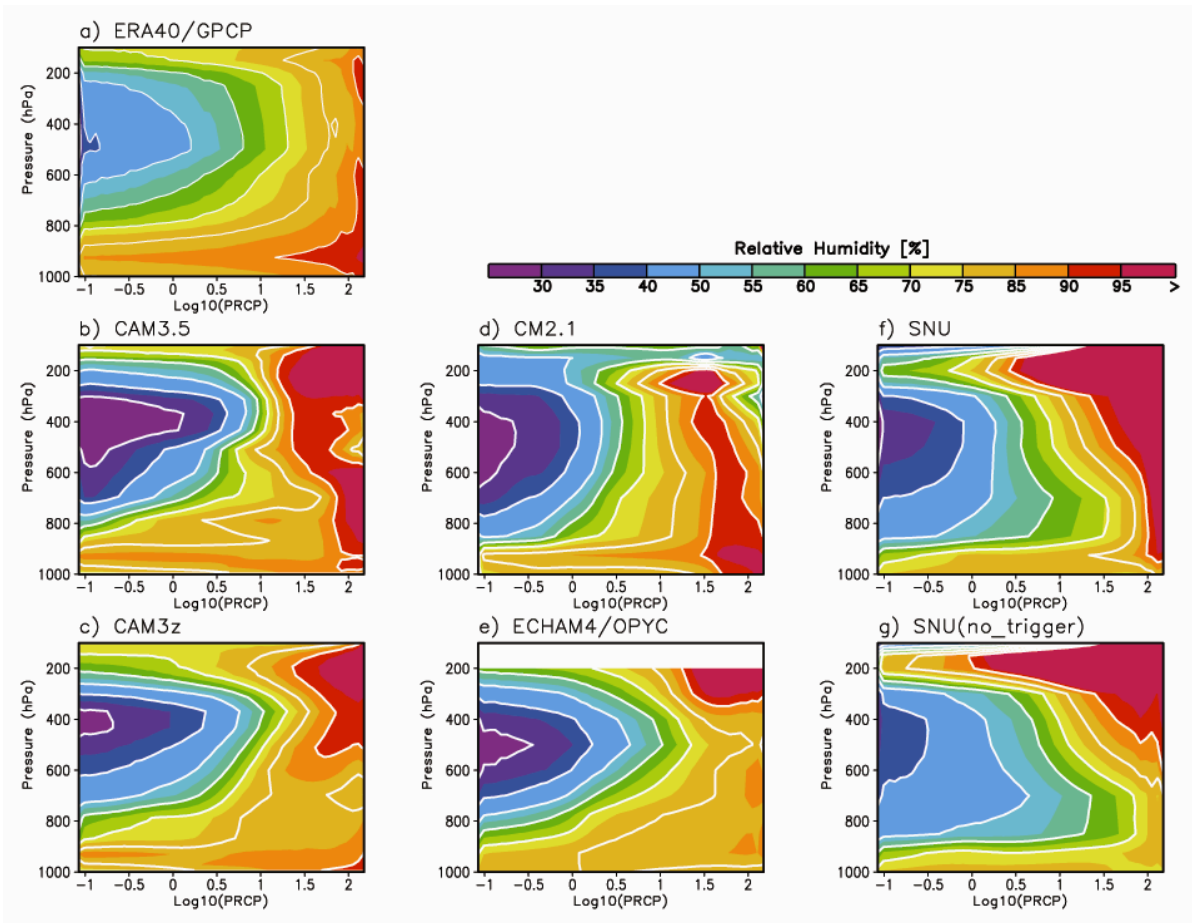


Figure 13. Composite vertical profile of relative humidity based on precipitation rate (a) ERA40/GPCP, b) CAM3.5, c) CAM3z, d) CM2.1, e) ECHAM4/OPYC, f) SNU, and g) SNU without convective inhibition function. The precipitation rate is plotted on a log scale) with the relative humidity averaged for each bin shown on the x-axis. The data is analyzed over 40°E-220°E, 10°S-10°N.

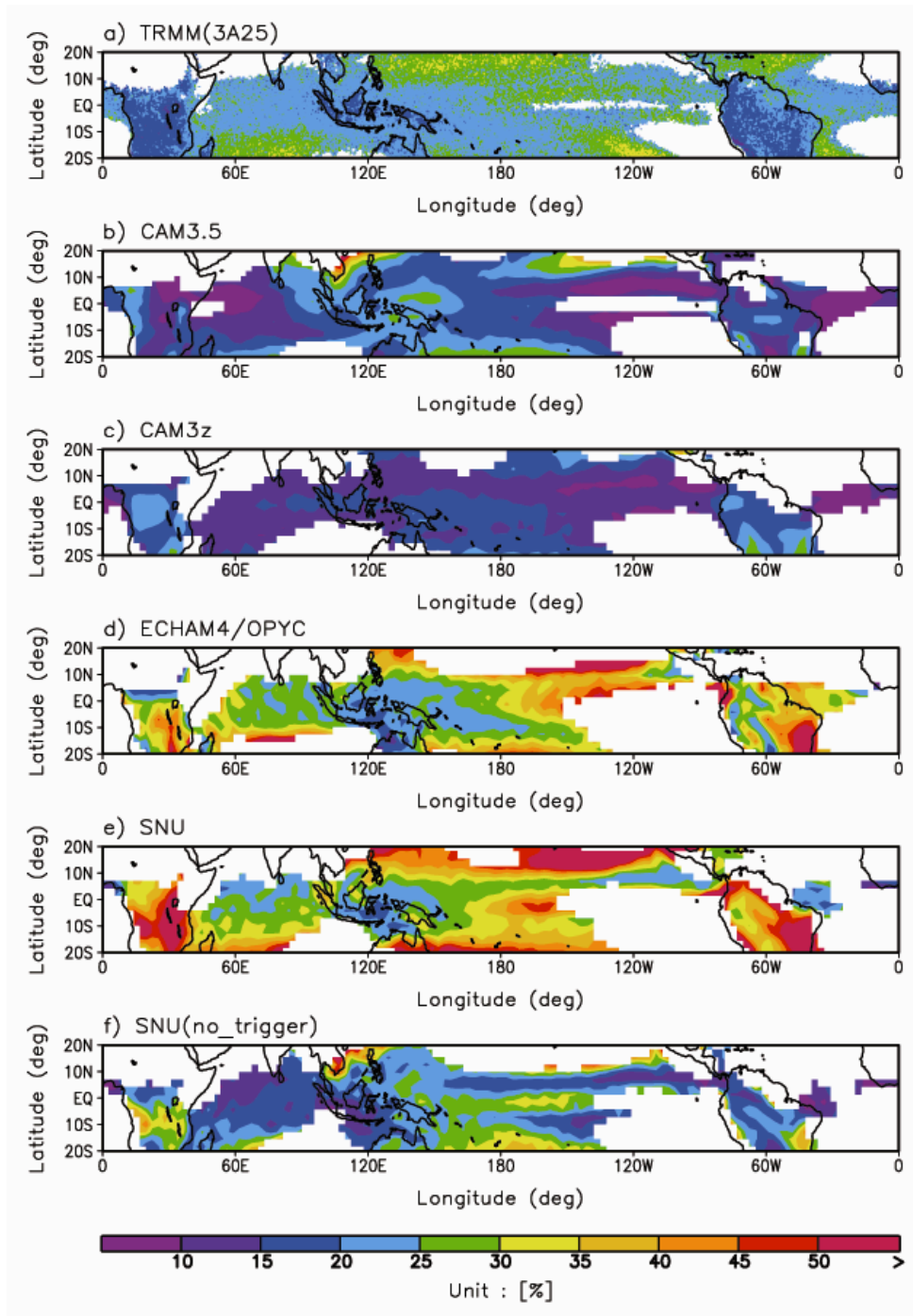


Figure 14. November-April mean stratiform rain fraction of a) TRMM 3A25 product, b) CAM3z, c) CAM3.5, d) ECHAM4/OPYC, e) SNU and f) SNU (no trigger). Areas with November-April mean rain of less than 2mm day^{-1} are not included.